Characterizing the potential energy of an atom trap through tomographic fluorescence imaging

Tanwa Arpornthip
Hatyai, Songkhla, Thailand

A.B., Washington University in St. Louis, 2009
M.A., University of Virginia, 2014

A Dissertation presented to the graduate faculty
of the University of Virginia in Candidacy for the Degree of
Doctor of Philosophy

Department of Physics

University of Virginia
December 2016

Thesis advisor: Professor Charles Sackett Tanwa Arpornthip

Characterizing the potential energy of an atom trap through tomographic fluorescence imaging

Abstract

We have developed a technique to fully characterize an arbitrary potential energy of an atom trap. The characterization allows one to measure the symmetry of the trap, a determining factor in many trapped atom applications. Created through a magneto-optical trap and evaporative cooling, a cold atom cloud is first loaded into our weakly-confined time-orbiting potential (TOP) trap. The whole atom cloud is then optically pumped into a dark state, an energy level that does not interact with the probe laser light. A selected part of the atom cloud is reactivated by a repump light which optically pump the atoms back into a state that can be probed. The repump light is shaped into a light sheet 168 μm thick. The reactivated region interacts with the probe laser light to create a fluorescence image. Since the light sheet is much thinner than the atom cloud, which is roughly 2 mm wide, the fluorescence image obtained is a cross-section of the atom cloud. A movable light sheet allows us to generate cross-section images of the cloud at different positions. A composite image of all the cross-section images shows the complete potential profile of our atom trap. This is similar to tomographic imaging used in medical imaging. We have verified the technique with two other methods: direct oscillation measurement at varying amplitude and numerical simulation of the atom trap. The technique is able to measure the potential up to the fourth-order terms in spatial coordinates. A complete characterization of the atom trap's symmetry will allow us to develop an atomic Foucault pendulum, a novel application for trapped atoms.

Acknowledgments

I would like to thanks many people who have helped me throughout my years in the program. Thank you, Prof. Cass Sackett, for being supportive and demanding simultaneously. Working with you has made me a better student, researcher, and teacher. For my dissertation committee members, Prof. Olivier Pfister, Prof. Tom Gallagher, and Prof. Bijoy Kundu, thank you for your time, knowledge, and your valuable suggestions for my dissertation. My colleagues have also been helpful throughout my time of study. I would like to thank Robert Horne, Bob Leonard, and Adam Fallon for the valuable discussion throughout my study. Special award goes to Eddie Moan who helped with data-taking and troubleshooting of the experiment. I would like to thank Holly Downs and her kids for being supportive of all my crazy ideas and providing me with entertainment when I needed it most. I would also like to thank the Seminole Trail Volunteer Fire Department's firefighters, especially my captain, Yousef Shakhsheer, who has set an example of how to work selflessly and tirelessly to improve our community in Charlottesville.

Last, and definitely least, I would like to thank the prospect of living in the US governed by President Trump. It did compel me to finish my work and to leave the country before he is sworn in.

Contents

List of figures

1

Introduction

Since the discovery of the Bose-Einstein condensate (BEC), many research applications have been proposed or studied [1]. In almost all applications, an atom trap is required to produce BEC. The potential created by an atom trap is one of the major factors dictating how successful an application with BEC can be. We propose a new application for trapped atoms, an atomic Foucault pendulum, that requires a highly symmetric atom trap. Our group has constructed an atom trap that can be adjusted to provide the symmetry. In order to so, a method to measure symmetry is needed. Our work here aims to provide a technique able to completely

characterize an atom trapping potential in three dimensions up to the fourth-order terms in spatial coordinates. The technique developed can also be used to improve other future experiments that we plan to implement in our atom trap.

In this introductory chapter, we will briefly discuss Bose-Einstein condensation. An analysis of the classical Foucault Pendulum and some of the obstacles in making one will be given. We will explain the similarities and the differences between an atomic Foucault pendulum and a classical Foucault pendulum, as well as our motivations in developing an atomic Foucault pendulum. A conceptual explanation of how an atomic Foucault pendulum works will be provided. To facilitate further discussion regarding involved atomic transitions in our experiments, a set of notations referring to different energy level of Rubidium atoms will be discussed. Lastly, the outline of the chapters in this dissertation is given.

1.1 Bose-Einstein condensate

To set the stage, we first discuss the nature of BEC and how it is produced. For a classical ideal gas, statistical mechanics can describe a system using Maxwell-Boltzmann statistics. When a system is at low temperature, the effects of quantum mechanics start to arise. In quantum mechanics, all particles are either bosons, those with integer spins, or fermions, those with half-integer spins. Fermions are forbidden from sharing a quantum state by the Pauli's exclusion principle. Bosons, on the other hand, are able to share a quantum state.

Because of this fact, bosons are able to undergo a special type of phase transition

known as BEC. The transition from a bosonic gas to BEC occurs when the de Broglie wavelength of the particles, λ_{dB}, becomes comparable to the inter-particle distance, $n^{-1/3}$, for atomic density n [2]. For a gas in equilibrium at temperature T, the thermal de Broglie wavelength is

$$\lambda_{dB} = \sqrt{\frac{2\pi\hbar^2}{mk_BT}} \tag{1.1}$$

where k_B is the Boltzmann's constant, $\hbar$ is the reduced Planck constant. Since the de Broglie wavelength depends on the temperature, we can recast the requirement for BEC transition as

$$k_BT(n) = \frac{2\pi\hbar^2}{m}n^{2/3} \tag{1.2}$$

where the dependence on the cloud density of the transition temperature is explicitly stated.

From Equation (1.2), we see that different experiments will have different transition temperature depending on the density of the atom cloud used. Another way to express the phase transition condition is through phase-space density. Phase space density is defined as the number of particles contained in a cubic volume with the sides equal to the thermal De Broglie wavelength.

$$\rho = n\lambda_{dB}^3 = n\left(\frac{2\pi\hbar^2}{mk_BT}\right)^{3/2} \tag{1.3}$$

The transition to BEC happens when $\rho \geq 2.612$, where a significant portion of the atoms occupy the ground state. In order to achieve the transition phase space density, a combination of density increasing and temperature reducing techniques are used [3].

Since the discovery of BEC, many applications have been developed or proposed: atomic clocks [4], gravimetry [5], Sagnac interferometer for rotation sensing [6], or, in our group, electric polarizability of Rubidium-87 measurement using a condensate interferometer [7]. For most of the applications, a trapping potential used to create a BEC and support the atoms against gravity has significant effect on the outcome of a measurement. An example is the dual Sagnac interferometer proposed by Horne [6]. In this interferometer, the atom cloud is split twice (see Figure 1.1). Each split produces two identical atom packets travelling in the opposite direction with the same momentum. The first split happens radially, which results in two atom packets travelling along the diameter of the potential trap (Figure 1.1a). Once the packets reach their turning points radially, the point at which their kinetic energy becomes zero, the atom packets are split again tangentially, creating two pairs of atoms (Figure 1.1b). To make a measurement, a recombination is needed for each of the pairs. In a symmetric potential, both atoms of a pair will return to their initial tangential split location after one period of oscillation, resulting in a high contrast interference signal. In an asymmetric trap, the two atoms will typically miss one another, rendering interference difficult, if not impossible. Asymmetry of the atom trap has negative impacts on the quality of the interferometer regardless of whether it is in the harmonic or anharmonic order. Anharmonicity also manifests as a phase shift in an atomic interferometer, which can mask the real phase shift caused by the phenomenon being studied [8].

We propose that an atom trap and a BEC can also be used to create an atomic Foucault pendulum. Having an atom trap with high-quality symmetry is critical to the construction of one. In order to fine tune the atom trap to achieve the required level

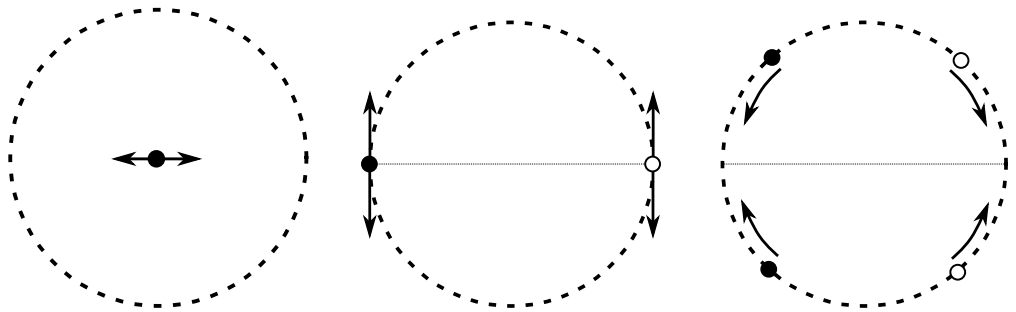

(a) Initial split **(b)** Tangential split **(c)** Trajectory for recombination

Figure 1.1: Diagrams showing the movement of atoms inside a dual Sagnac Interferometer. The large dashed circle shows an equipotential surface at the turning point for the atoms. First, in Figure 1.1a, with the atom cloud at the origin, a radial Bragg split is initiated. The split atoms move until they reach the turning point radially, at which point two tangential splits are performed, as shown in Figure 1.1b. The four atom packets move around the equipotential surface in a circular orbit in Figure 1.1c. If the atom trap is symmetric, the location of each atom packets in the same pair will coincide at the tangential split location, allowing us to recombine them and achieve an interferometer. On the other hand, if the atom trap is not symmetric, the packets in a pair can miss one another.

of symmetry, a new technique has to be developed to study the potential energy of the atom trap in 3D, as an atomic Foucault pendulum can be implemented for an arbitrary rotation not limited to a plane, unlike its classical counterpart. The technique developed has to be capable of characterizing the atom trap up to at least the fourth-order terms in spatial dependence. Our work here will show that we have developed a technique, fluorescence tomographic imaging, that satisfies both requirements.

Despite the importance of the trapping potential energy shape on the measurement result, methods for a complete three-dimensional characterization of the potential have received little attention. When a method is presented, it usually involves extra laser and optics components which make the experiment more complicated. For example, Brantut uses a probe beam at different detuning to develop a light shift tomography of atoms trapped in a dipole potential trap [9]. Our technique requires minimal extra laser and optics.

1.2 Classical Foucault pendulum

Since its first public appearance in Paris in 1851, the Foucault pendulum has captivated the interests of the public [10]. The seemingly magical rotation of its oscillation plane was the first terrestrial-based experiment to irrefutably show that the Earth spins around like a top [11]. While the motion of the Foucault pendulum relies entirely on classical mechanics, there are various ways to explain the phenomenon [12, 13, 14, 15]. Even though the initial discovery and explanation were conceived in 1851, the relevance of Foucault pendulum in various fields can still be seen to this day [16, 17]. While there are some efforts to expand the concept to different systems [18, 19], to our best knowledge, the application of a Foucault pendulum in atomic regime is absent.

As Baker et al. elegantly put, all pendulums are Foucault pendulums. However, the Foucault effect is often masked by other types of motion in the pendulums. The masking renders common pendulums useless in demonstrating Earth's rotation. To be more specific, a Foucault pendulum is a pendulum that is well-designed and well-tuned to show the rotation of the pendulum's oscillating plane [11].

Qualitatively, the Foucault effect is easily understood. Imagine yourself floating in space right above the North pole of the Earth, where your friend, Eddie, is located. On the North pole, a large pendulum, properly sized so you can see it from your position in space, is installed. The pendulum is set to swing back and forth in a line. Let's call the line of swinging the oscillation plane. Initially, the plane of oscillation will point along one specific longtitude line. If the pendulum is so well-built such that it doesn't lose its motion through friction from its hanging point or air drag, it can be observed

for a long period of time. For a long observation, the oscillation plane of the pendulum appears stationary to you, an observer floating in space. However, the supporting structure and the ground underneath the pendulum slowly rotates with Earth's rotation. To you, the phenomenon makes intuitive sense. You can clearly see the Earth's rotation and the initial longitude line slowly rotates away from the pendulum's oscillation plane. On the other hand, Eddie, standing next to the pendulum, is rotating with the Earth. To him, the pendulum's support structure and the Earth are standing still, while the Foucault pendulum slowly rotates away from its initial longitude. In fact, if both observers wait long enough, it will take exactly 24 hours for the pendulum and the Earth to revert back to their original conditions. The same experiment can also be performed on the South pole with similar result. The same experiment performed on the equator is null. The pendulum's plane of oscillation moves with the Earth's rotation; there is no relative rotation between the pendulum and the ground underneath (see Figure 1.2).

For other places between the equator and the two poles, the effect varies depending on the latitude of the pendulum location. For a Foucault pendulum situated at latitude β, the Foucault pendulum's oscillation plane will make a complete revolution in time T,

$$\mathrm{T} = (24 \text{ hours}) / \sin\beta \tag{1.4}$$

Readers who are interested in a more in-depth explanation of the effect can consult many standard classical mechanics textbooks [21, 22, 23].

While Foucault pendulums are conceptually easy to understand, constructing one

is anything but easy. Baker et al. provide an exhaustive list of the factors effecting the quality of the Foucault effect in a pendulum [11]. A quick summary is provided here. There are three major factors that determine the quality of a Foucault pendulum.

First, the initial velocity of the pendulum defines the plane of oscillation. The direction of the initial velocity dictates how well the Foucault effect can be observed. Any amateur who has ever tried to imitate Rocky Balboa punching a boxing speedbag learns quickly the importance of pushing the speedbag strictly forward and backward. The angle at which the fists hit the bag dictates the following motion of the speedbag. For maximum satisfaction and the most rapid bounces, the speedbag should travel only in the direction facing the boxer. If the bag is punched at an off angle, an undesirable effect in which the bag makes a circular motion around its hanging point makes the boxer lose the rhythm. That is, the motion of the bag needs to contain only velocity in the same line as the bag's displacement. Similarly, for a precise and well-defined plane of oscillation, a Foucault pendulum has to be released without imparting a velocity in the direction perpendicular to the initial displacement. Failure to do so will result in the pendulum exhibiting an elliptical orbit, instead of a line, even in the absence of Earth's rotation. This non-linear trajectory can mask the Foucault effect. The problem of releasing the pendulum is important enough to be its own subject of study. Many pendulum-releasing methods have been tried, including mechanical releases and magnetic releases. The method in-

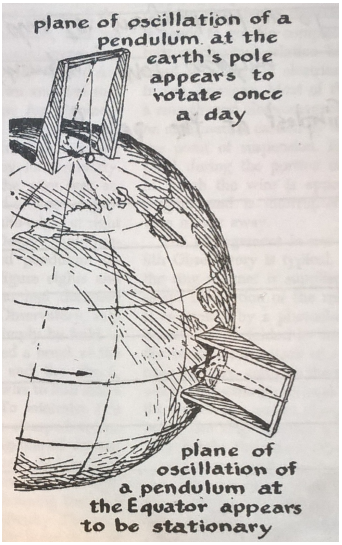

Figure 1.2: Diagram showing Foucault pendulums at different point on Earth. Diagram taken from [20]

vented by Foucault, a candle burning through a light thread that holds the pendulum bob in place at its maximum displacement, still remains one of the most elegant and simplest methods [20]

Second, an asymmetry in the bob's oscillation plane damages the quality of a Foucault pendulum. An oscillation of an ideal Foucault pendulum has no preferred direction of motion. In other words, any initial release of the pendulum, as long as no perpendicular velocity component is present, results in an oscillation plane. Any oscillation planes can be expressed as a linear combination of two fundamental oscillations that are mutually perpendicular. The two fundamental oscillation directions are called the principal axes. The pendulum is cylindrically symemtric when both fundamental oscillations have the same oscillation frequency. In reality, unless extreme care has been taken or correcting devices have been installed, a pendulum exhibits oscillation frequency differences between the two principal axes. An oscillation not aligned with a principal axis becomes a linear superposition of two oscillations with the two different fundamental frequencies. As a superposition of two oscillations, the trajectory continuously changes from a line along the first principal axis, to an ellipse, to another line along a different axis and back. The frequency of the shape change is proportional to the difference in the fundamental oscillation frequencies.

Thus, a pendulum without radial symmetry cannot exhibit the Foucault effect. The change in the trajectory shape in an asymmetric Foucault pendulum conceals the much smaller Foucault motion. In fact, multiple anecdotes have been told about the extreme measures used to achieve cylindrical symmetry or the ease at which the symmetry can be destroyed. For example, the wire for the Foucault pendulum hung in the

Griffith Observatory, Los Angeles, California, was made overseas. To prevent coiling the wire and introducing an unbalanced bend, the wire was strung across a custom built container while in shipment [20]. Foucault pendulums located in stairways of museums suffer from an imbalance of traffic going up or down the stairs. Doors and windows have to be closed to prevent air draft on the pendulums [24]. Figure 1.3 shows examples of trajectories in pendulums with various degrees of symmetry.

Third, the amplitude dependence of the oscillation period can create an effect that masks or cancels the Foucault effect. In the lowest order of approximation, the period of oscillation is independent of the oscillation amplitude. The next order of approximation, however, shows that the period of oscillation shifts proportionally to the square of the amplitude, as

$$T \sim T_0 \left[1 + \frac{\alpha^2}{16}\right] \tag{1.5}$$

where T_0 is the small amplitude oscillation period and α is the amplitude of the oscillation, in radians. This effect is known as the anharmonicity of the pendulum. Since the Foucault effect introduces a small velocity component in the direction perpendicular to the pendulum plane of oscillation, even in a perfectly symmetric Foucault pendulum, the trajectory is a small ellipse. Due to the amplitude dependence, the pendulum's period along the semi-major axis of the ellipse is longer than the semi-minor axis. The anharmonicity causes the pendulum's motion to start veering. The veering of the pendulum created by anharmonicity can create systematic error in measuring the Foucault effect. To reduce the anharmonicity effect, the oscillation amplitude should be kept small.

In the lowest order of approximation, our atom trap for BEC creates a potential that resembles that of a classical pendulum. Theoretically, we should be able to create an atomic Foucault pendulum using oscillating trapped atoms and their plane of oscillation. While we feel this observation would be interesting in its own right, an atomic Foucault pendulum could also serve as a rotation sensor. The Foucault effect arises regardless of the cause of the rotation. While a Sagnac interferometer can sense small rotation very precisely, large rotation increases the phase difference to larger than 2π. The measurement of phase difference beyond 2π for an interferometer is difficult to interpret. On the other hand, an atomic Foucault pendulum provides a direct measurement of rotation angle, which makes it an ideal measurement to track large rotation.

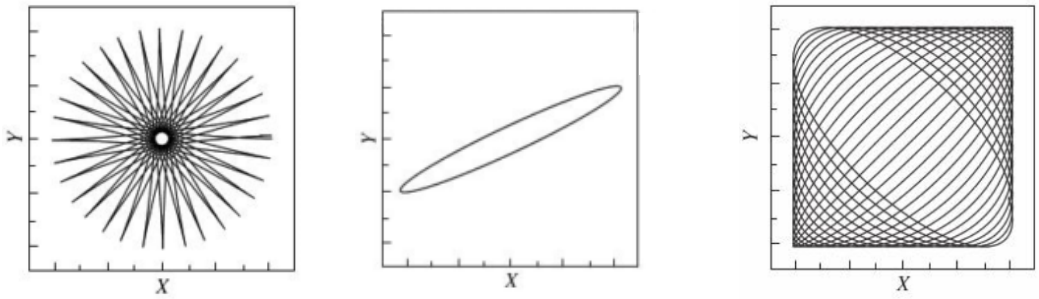

(a) Foucault pendulum motion

(b) Bad pendulum release

(c) Trajectory changes in asymmetric pendulum

Figure 1.3: Figure 1.3a shows the trajectory of a Foucault pendulum, with the effect greatly exaggerated. Figure 1.3b shows the trajectory of the pendulum when the initial velocity is not directed along the same line as the displacement. The result trajectory is elliptical. Figure 1.3c shows the cyclical fattening and thinning of an elliptical trajectory due to the asymmetry between the two principal axes. The elliptical orbit gradually fattens until it becomes a circle, and then another ellipse. The cycle is then reversed. All figures are from [11].

1.3 Atomic Foucault pendulum

In this section, we will explain the underlying principle of an atomic Foucault pendulum. The similarities and differences between a classical Foucault pendulum and an atomic Foucault pendulum will be shown. Selected reasons for developing an atomic pendulum will be discussed.

While a classical Foucault pendulum is a marvelous measuring device, an atomic Foucault pendulum has many advantages. First, a classical Foucault pendulum occupies a large volume. Having a long pendulum arm allows the Foucault effect to be easily observed in a classical Foucault pendulum. A long pendulum arm also increases the tolerance for asymmetry. The Foucault pendulum in the Pantheon, Paris, has a cable that is 97 metres long [11]. On the other hand, an atomic Foucault pendulum has the potential to be miniaturized. A miniaturized version can be installed in space-limited experiments: space stations, airplanes, underwater vessels, etc. There are already multiple efforts to miniaturize an ultracold atom system [25, 26].

Second, an atomic Foucault pendulum can sense rotation in an arbitrary direction. The potential for an atomic Foucault pendulum is provided by an atom trap that can be designed to provide desired potential shapes. Consequently, an atom trap can be designed to possess spherical symmetry. The increased symmetry allows such a trap to sense rotation in an arbitrary direction. The classical Foucault pendulum can detect the rotation in only one direction, along the straight line between the bob and the hang point when the bob is at rest. Since the oscillation is not limited to a plane by physical requirements, a spherically symmetric potential allows an arbitrary rotation

vector to exhibit the Foucault effect. Note that an atom trap with spherical symmetry has been reported in the past [27]. However, the degree of symmetry (about one percent oscillation frequency fluctuation in all directions at 7.8 Hz) achieved was not sufficient to implement an atomic Foucault pendulum. Our atom trap can achieve the same level of accuracy at a smaller oscillation frequency of 1.3 Hz. While an atomic Foucault pendulum with spherical symmetry is more desirable, for simplicity, we choose to limit our proof-of-concept experiment to horizontal cylindrical symmetry.

Third, unlike the classical version which is plagued by multitude of unpredictable problems and extraordinary precautions as described in Section 1.2, interactions of atoms with the environment is better understood and more predictable. An atomic pendulum will most likely be implemented in a vacuum cell, which help insulates it from external interferences. Some of the external interferences for an atomic pendulum are optical (stray laser light, background scattering), electromagnetic waves (background magnetic field, stray radio signals), and gravity. The interactions of the atoms with the external interferences have been studied to a much greater extent than the interferences that could effect a classical Foucault pendulum.

Not only does an atomic Foucault pendulum potentially have more advantages than its clasical counterpart, the various requirements, especially the high-quality cylindrical symmetry, needed for a successful application help us understand and better develop other cold atom applications in our atom trap. For example, a high-quality cylindrical symmetry will allow us to implement a better dual Sagnac Interferometer with adjustable enclosed area.

1.4 Conceptual explanation of an atomic Foucault pendulum

In this section, we will explain how an atomic Foucault pendulum works without mentioning specific implementations or apparatus design. The concepts introduced in this section should be applicable to any kind of atom traps, as long as they possess the right symmetry for a Foucault pendulum. Our implementation and apparatus design will be covered in Chapter 2.

In order to have a pendulum, a restoring force is needed. In a classical pendulum, the string's tension and the gravity acting on the pendulum bob create an approximate harmonic potential for small oscillations. For an atomic Foucault pendulum, an atom trap can generate a trapping potential on the atoms. Analogous to rolling a marble in a salad bowl, the trapped atoms, if displaced from the minimum potential point, will oscillate in the bowl. The trajectory of the oscillation depends on the initial conditions of the atoms and the shape of the bowl. The initial conditions of the atoms will be discussed later in this section. The potential created by the trap, the shape of the salad bowl, is shaped through a careful design of the trap. The potential generated from the trap can be designed to have the necessary qualities to make a Foucault pendulum: cylindrically symmetric with negligible anharmonicity.

The motion of the bob in a classical pendulum defines the oscillation trajectory. In an atomic pendulum case, we have two options for tracking the trajectory. One, the entire trapped atom cloud can be made to oscillate in the trapping potential. A series of time-based images can be taken and combined to extract the trajectory. The series of images is equivalent to recording the position of the classical pendulum's bob as a

function of time. Two, the trapped atoms can be split into multiple packets: one stationary and the rest moving with the moving packets making up pairs. Each packet in a pair is sent out with the same initial speed but in the opposite direction. The stationary packet remains at the trap center at all times. Unless taken when all the packets are aligned on top of one another while passing the center of the trap, a single image can determine the plane of oscillation. A schematic diagram of this method is shown in Figure 1.4. Both of these methods will be discussed further in Section 2.3.

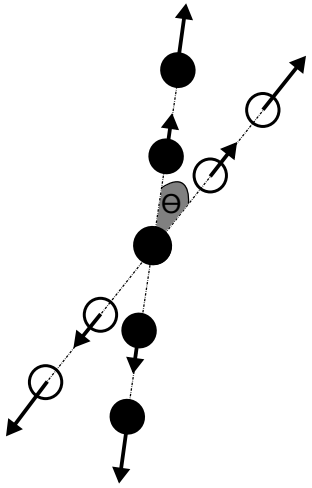

Figure 1.4: A diagram showing the Foucault effect in an atomic pendulum in which the atom cloud is split into multiple packets. The length of the vectors indicate packet's velocity. The hollow circles represent initial line of oscillation, while the filled circles show the position of the same packets at a later time. The center packet remains stationary at the trap's potential minima at all time. The Foucault effect rotates the plane of oscillation by Θ.

To measure the Foucault effect, the plane of oscillation is measured using one of the methods described above. The initial plane of oscillation is compared to the one from later measurement. The Foucault effect manifests in the rotation of the oscillation plane. Since the source of rotation can come from Earth's motion, or the rotation of the atomic pendulum's apparatus, the atomic Foucault pendulum can be used as a rotation sensor device.

1.5 Rubidium energy level notations

Our implementation of atomic Foucault pendulum uses Rubidium atoms. Throughout this dissertation, we will refer to selected energy levels of Rubidium atom, the transitions between

the energy levels stimulated by the laser beams, and laser beams designed to perform specific tasks. For brevity, we will define shorthand notations for these entities.

To describe the electronic configuration of an atom precisely to the hyperfine structure, spectroscopic notation is used. In general, a complete information about an electron can be expressed in the following form

$$\mathrm{n}^{2\mathrm{s}+1}\ell_{\mathrm{J}} \quad \mathrm{F} \quad \mathrm{m} \tag{1.6}$$

where n is the principal quantum number. $2\mathrm{s}+1$ is the spin multiplicity. ℓ is the total orbital angular momentum. J is the total angular momentum from both the electron's orbit and spin. The F and m quantum numbers give the hyperfine state of the atom. For example, an energy level of a Rubidium atom might be $5^2\mathrm{S}_{1/2}$ F = 1, m = 2. The hyperfine structure is caused by the coupling between the angular momentum of the electron and the nucleus's spin. F is the total angular momentum of the coupled electron and nucleus. m is the magnetic Zeeman quantum number for the total spin projected along a chosen axis. See Figure 1.5 for the diagram of the energy levels involved in spectroscopic notation.

In our experiment, the electron makes transition between two states: $5^2\mathrm{S}_{1/2}$ and $5^2\mathrm{P}_{3/2}$. Since there are only two fine structure states used, we can shorten the spectroscopic notation further. Any primed hyperfine notations refer to the $5^2\mathrm{P}_{3/2}$ state, while the unprimed ones refer to the $5^2\mathrm{S}_{1/2}$ state. For example, $5^2\mathrm{S}_{1/2}$ F = 1 becomes F = 1 and $5^2\mathrm{P}_{3/2}$ F$'$ = 3, m$'$ = 2 becomes F$'$ = 3, m$'$ = 2. Figure 1.5 also shows the transitions involve in the experiment. The transitions shown are only the excitation transi-

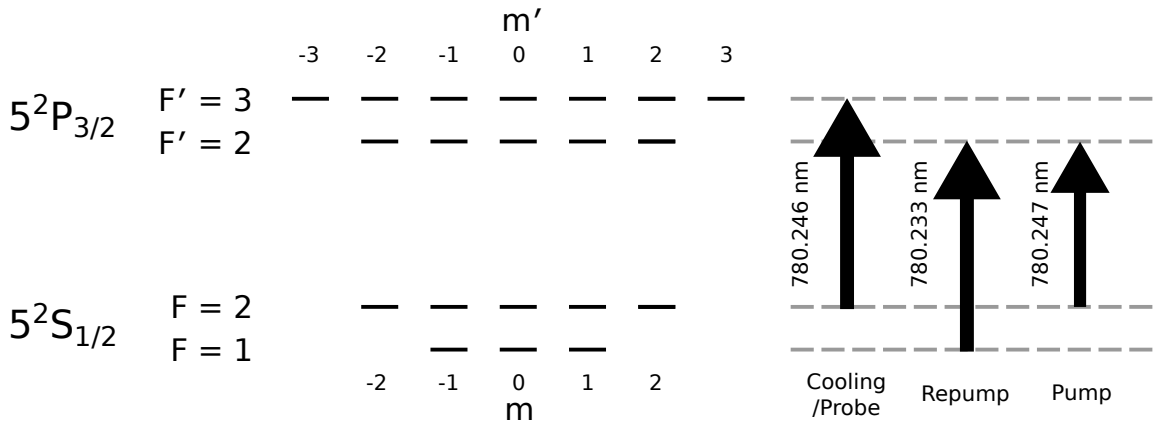

Figure 1.5: Diagram showing all the energy levels of Rubidium involved in the experiment, as well as the wavelengths and corresponding transitions of the laser beams. In this dissertation, prime symbols always refer to the $5^2P_{3/2}$. The unprimed symbols refer to the $5^2S_{1/2}$. The value of F and m will be specified when relevant.

tions, an electron being excited into a higher energy level. The relaxation transitions will be discussed in the sections where they become relevant.

1.6 Scope

The scope of the dissertation is to present a technique to measure the potential profile of an atom trap created by Horne [6]. The fluorescence-based tomographic technique developed is able to measure the potential profile in three dimensions up to the fourth-order terms in spatial coordinate dependence. In discussing the trapping potential profile, we will refer often to our goal to create an atomic Foucault pendulum. The dissertation consists of five additional chapters beyond the current introductory chapter.

> **Chapter 2: Atomic Foucault Pendulum**: In this chapter, we discuss the implementation of an atomic Foucault pendulum. The concept for an atomic Foucault pendulum is discussed. The apparatus, including the science trap in our experiment, is described. The detection of the trapped atoms and how to observe

the oscillatory behavior are presented. The different choices in creating oscillatory motion in the trapped atoms and the conditions for using each of them are discussed. The analysis of the atoms' trajectory is provided.

Chapter 3: Measuring the potential: In addition to the trajectory analysis presented in chapter 2, a tomographic technique to measure the trapping potential profile is shown. Tomography is a technique used to obtain cross-sectional information from a 3D object. In our case, the 3D object is the atom cloud, from which the potential can be obtained. The additional equipment needed for tomographic imaging is discussed. The analysis of tomographic slices is presented, as well as its mathematical model. The temperature of the atom cloud is measured.

Chapter 4: Harmonic terms: In the lowest order approximations, the trapped atoms' behavior is governed by the harmonic terms, the terms in the potential proportional to the square of the spatial coordinates. The importance of well-balanced harmonic terms for a successful atomic Foucault pendulum is discussed. The deviation from an off-balance harmonic terms and the consequences are discussed. The theoretical and empirical evidence showing balanced harmonic terms are presented. The allowable level of harmonic asymmetry is discussed.

Chapter 5: Anharmonic terms: Beyond the harmonic terms, the trapping potential has anharmonic terms, the terms in the potential that change more rapidly than the square of the spatial coordinates. The effects of the anharmonic terms on the atoms' motion are discussed. The tomographic technique presented in Chapter 3 is used to measure the trapping potential profiles. The result of the tomographic measurement is verified by comparing it to similar values obtained through oscillation measurement and numerical simulation. The 3D reconstructed model of the trapping potential from the tomographic data is presented.

Chapter 6: Conclusion: We will summarize the tomographic technique we have developed. While asymmetry in the anharmonic terms will be a challenge for the development of an atomic Foucault pendulum, we will discuss some techniques by which they could be controlled.

2

Atomic Foucault Pendulum Apparatus

Our BEC apparatus is adapted to implement the atomic Foucault pendulum. In this chapter, the specifics of our apparatus and how we aim to create an atomic Foucault pendulum will be discussed. we will describe the techniques used to induce atom oscillation, atom detection system, and the method we use to analyze atom motion.

2.1 Apparatus description

In this section, we will discuss the specifics of our apparatus and how we aim to create an atomic Foucault pendulum. Our atomic "bob" is a Bose-Einstein condensate (BEC). First constructed by Horne [6], our adjustable science trap, a type of a magnetic atom trap, provides the trapping potential. To make the entire cloud of trapped atoms oscillate, we install a magnetic coil, the "kick coil", capable of displacing the center of the magnetic atom trap. To separate the trapped atoms into multiple packets, a laser is used to create a standing optical wave on the atoms causing the atoms to split with predictable momentum, a phenomenon called Bragg scattering. We will also mention how to create a cold atom cloud, which is hotter than the BEC. The cold atom cloud is used in characterizing the trap's potential energy, a topic that will be discussed later in Chapter 3. The discussion here provides a brief overview of the apparatus and the process of creating a cold atom cloud. The apparatus and the process are discussed in more detail in Horne's thesis [6]. In general, our procedure for creating a Bose-Einstein condensate largely follows the methods described in [28].

As discussed in Section 1.1, to produce a cold atom cloud or a Bose-Einstein condensate (BEC), we have to decrease the temperature of the atom cloud.

2.1.1 Initial cooling of atoms

We use Rubidium (Rb) atoms in our experiment. Rubidium is an alkali-metal, a class of elements that is suitable for atom trapping for various reasons: conveniently-accessible transition frequency, simplicity of electronic configuration, and ease of sourcing [29].

We source our Rb atoms using four alkali metal dispensers (SAES, Rb/NF/3.4/12/FT 10+10). The dispensers are wired into two pairs, each with two dispensers connected in series. We only run a single pair at a time. A single pair of dispensers typically lasts about 1.5 - 2 years, depending on the amount of use. We install the second pair of dispensers to lengthen the amount of time before we have to break the vacuum seal of the system to replenish our Rb supply. The amount of Rb dispensed is a function of time and temperature. Typical dispensing rate is about 1 μg per minute. The latter can be controlled by adjusting the amount of current going through the dispenser.

Since our Rb source produces hot and fast-moving atoms, we need to significantly cool the atoms down before we can load the atoms into our magnetic atom trap. Without pre-cooling, the atoms would be too hot to remain in the trap at all. There are many methods to achieve this result. The two most common methods are the Zeeman slower [30] and the magneto-optical trap (MOT). We employed the latter to initially capture and cool down the atoms.

The MOT has become the one of the most widely-used tools in cold atom physics. It was invented in 1991 by Chu et al. [31]. The most common geometry of a MOT consists of three pairs of counter-propagating laser beams and a quadrupole magnetic field. In our case, we use a field with the gradient of 10 G/cm along the z-direction [6]. All the laser pairs are mutually orthogonal. All three pairs intersect at the zero location of the quadrupole field [32]. The use of carefully selected polarization and detuning imparts spatially dependent forces on the atoms, directing them towards the zero field location and creating an atom trap.

As shown in Figure 2.1, our experiment uses two vacuum chambers: the MOT

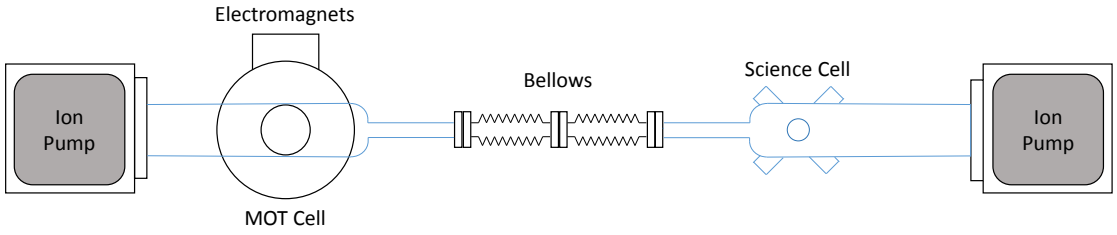

Figure 2.1: Schematic diagram of the experiment. Diagram taken from [6].

cell and the science cell. The vacuum in both cells is maintained by ion pumps and a Titanium sublimation pump. A tiny fraction of the atoms released by the dispensers are captured using a magneto-optical trap in the MOT cell. We typically capture 10^9 atoms at roughly 150 μK [6].

For an ideal two-level atom, only a single laser is needed to create a MOT. Since Rubidium has multiple energy levels, two lasers are needed. Figure 1.5 shows the relevant energy levels and laser transitions. See Figure 2.2 for possible transitions and their probabilities. The first laser, called the cooling laser, is tuned to the transition that is calibrated for magneto-optical trap effect. When the atoms interact with the cooling laser, the majority of them are excited to the $F' = 3$ level. However, an appreciable fraction of atoms can also populate an alternate state $F' = 2$. While all of the atoms populating the $F' = 3$ state decay down to the ground state $F = 2$, atoms in the $F' = 2$ state can decay to either the $F = 2$ or $F = 1$ state. Those atoms decaying back into the $F = 2$ state go through the MOT process again. Atoms decaying into the $F = 1$ state no longer interact with the cooling laser and go dark. With no remedy, eventually, all the atoms will be "pumped" to the dark $F = 1$ state. The second laser, the repump, is tuned to the $F = 1 \rightarrow F' = 2$ transition. The repump laser take atoms out

of the dark state and put them back into the F = 2 to F′ = 3.

The achievable atomic density is limited to about $10^{11}/\text{cm}^2$ in a MOT [29], because the atom cloud becomes optically dense and the cooling light cannot reach the center of the cloud. Some examples and further details on MOT limitations can be found in [34, 35]. To increase the density of the atom cloud beyond this limit, a compressed magneto-optical trap (CMOT) is used to increase the density of the cloud. Two modifications are needed.

First, the frequency of the cooling laser is changed. During the regular MOT, the cooling laser is tuned 20 MHz red of the cooling transition. Deliberately tuning the laser frequency slightly away from an atomic transition is known as detuning. For the CMOT, the cooling laser is detuned further, to 60 MHz red of the cooling transition. The rate at which an atom scattering a laser light depends on this detuning. In general, the scattering rate of an atom illuminated by a laser light with intensity I and detuning Δ is

$$R_s = \frac{\Gamma}{2}\left(\frac{I/I_s}{1 + I/I_s + 4\Delta^2/\Gamma^2}\right), \tag{2.1}$$

where R_s is the scattering rate, Γ is the natural linewidth of the transition, and I_s is the saturation intensity of the transition. As detuning increases, atoms scatter fewer photons. The greater detuning during the CMOT allows the cooling photons to penetrate deeper into the dense atom cloud. The penetration increases the chance that the interior of the cloud receives the benefit of the cooling effect.

Second, the repump beam power is reduced by roughly 50%. With less repump light, when an atom falls into the F = 1 dark state, it will take longer for the atom to

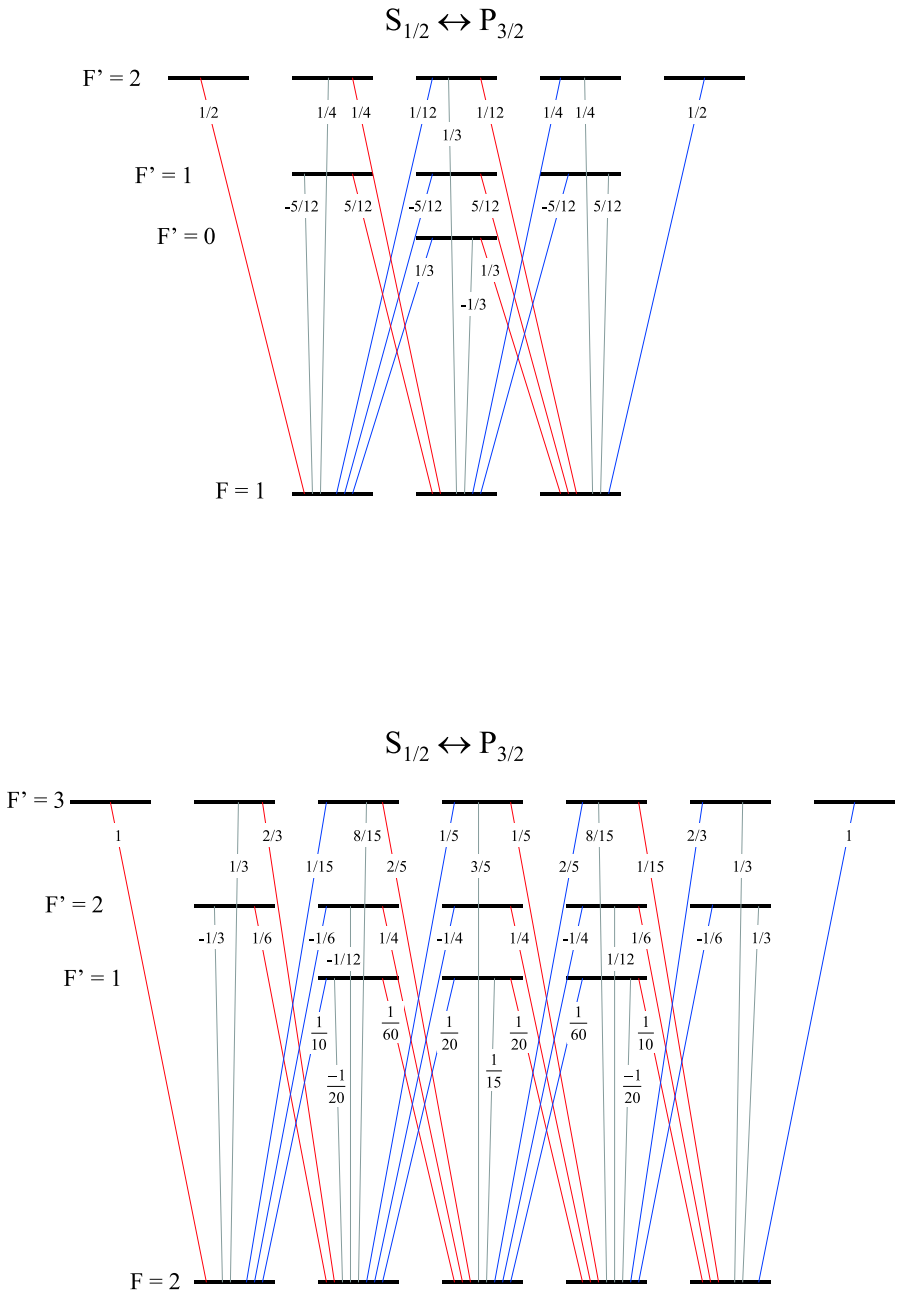

Figure 2.2: Coupling constants of various transitions of 87Rb relevant to the experiment. Figure and data taken from [33]

receive a repump photon. Spending more time in the dark state, an atom interacts less with the cooling light. This further reduces the optical density of the cloud. Since the atoms are already cold, the corresponding reduction in the cooling force is not important.

2.1.2 Optical pumping and magnetic trap

After the CMOT, the lasers are turned off and the atoms return to the F = 2 state. The next step is to load the atoms into a magnetic trap. An atom in a magnetic field experiences an energy shift due to the Zeeman effect, which is proportional to the inner product of the atom's magnetic monent and the magnetic field:

$$U = -\vec{\mu} \cdot \vec{B} \tag{2.2}$$

where μ is the magnetic moment of the atom. In a particular Zeeman state m_F, the angle between $\vec{\mu}$ and $\vec{B}$ is fixed. In this case, the potential energy becomes

$$U = g_F m_F \mu_B B \tag{2.3}$$

where g_F is the Landé g factor of the hyperfine level F, m is the magnetic quantum number, and μ_B is the Bohr magneton. Atoms can be trapped in a magnetic field with either a maximum or a minimum, depending on the signs of the g-factor and m_F. For a positive $g_F m_F$, the potential is minimized at a field minimum. Such atoms are called low-field seeking. On the contrary, a negative $g_F m_F$ results in high-field seeking atoms.

The g-factor can be found in the literature [36]. Since a local magnetic field maximum is not possible in free space [37], only low-field seeking atoms are trappable.

The same anti-Helmholtz coil used for MOT is used to generate a spherical quadrupole field with field zero at the trap center. The magnetic field generated by the coils is

$$\vec{B} = B'\left[\frac{1}{2}(x\hat{x}+y\hat{y})-z\hat{z}\right] \tag{2.4}$$

$$|\vec{B}| = \frac{B'}{2}\sqrt{x^2+y^2+4z^2} \tag{2.5}$$

which has the zero-field location and a global minimum at the origin, where the low-field seeking atoms are trapped. The field gradient B' used in the spherical quadrupole trap is 388 G/cm at maximum coil current of approximately 750 A [6]. The coordinate axes are defined as shown in Figure 2.3. The spherical quadrupole field produced has a gradient that changes linearly in all x, y, and z-directions, but the z-direction gradient's rate of change is doubled.

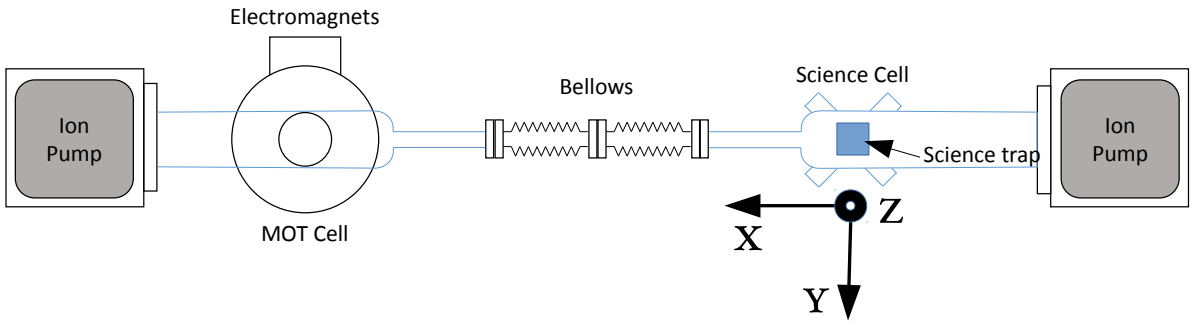

Figure 2.3: Apparatus diagram with the science trap's location and axes labeled. The diagram was modified from [6]. The Z-axis points out of the plane at the reader.

For the F = 2 state, $g_F = 1/2$. Because of the positive g-factor, the potential for

the atoms is minimized at the field minimum location for the substates with positive m_F. Consequently, Rb atoms in F = 2 $m_F = +1, +2$ states are trappable at the field minimum point. The trapping force on the atoms is proportional to the negative gradient of the potential.

$$\vec{F} = -g_F m \mu_B \vec{\nabla} B \tag{2.6}$$

We see that the trapping force is linearly proportional to the magnetic quantum number of the atom. Since the atoms distribute themselves in all substates after the CMOT, with no further modification, we stand to lose a large portion of atoms. To gather as many atoms as we can, we want to transfer all the atoms to a trappable substate. We use a process called optical pumping, which steps the atoms through each substate with progressively increasing spin until all the atoms has the maximum spin possible ($m_F = 2$).

The optical pumping process is shown in Figure 2.4. After the CMOT, the MOT magnetic field is turned off. A small uniform "bias" magnetic field is then turned on to establish a spin quantization axis for the atom. To understand the pumping mechanism, consider an atom that is in the F = 2, m = 0 state. A laser pump beam tuned 25 MHz red of the F = 2 $\rightarrow$ F$'$ = 2 transition illuminates the atoms. The pump beam has σ^+ with respect to the small "bias" magnetic field. The polarization of the pump beam induces only transitions that increase m. Since the pump beam always increase the magnetic quantum number by one, the atom is excited to the m$'$ = 1 state. Once excited, it can either decay down to the F = 2 or F = 1 state. If it decays to the F = 1 state, it is transferred back to the F = 2 state by the repump light. Once in F = 2,

it interacts with the pump beam again and gain an additional magnetic quantum number. During the emission process, the magnetic quantum number m can change by -1, 0, or $+1$, giving zero effect on average. Since the contribution from the pumping transition is always positive, the atom steps through the m-levels of the ground state with increasing magnetic quantum number until it reaches the $m = 2$. In this state, the atom becomes transparent to the pump beam as it cannot be excited up to the non-existent $m' = 3$ substate. We can transfer about 75% of the atoms to the $m = 2$ state by this process.

2.1.2.1 Atom transportation and final cooling

After optical pumping, the spherical quadrupole field is turned on quickly to capture the atoms. The spherical quadrupole trap is turned on by running the maximum current of 750 A through the quadrupole coil pair. Once loaded into the spherical quadrupole trap, the atoms are transferred from the MOT vacuum cell to the science vacuum cell. Without transferring the atoms to the science cell, background collision in the MOT cell reduces the lifetime of the atoms in the spherical quadrupole trap to roughly 10 seconds, a duration too short for our measurement. Due to the high rate of background loss, obtaining a BEC in the MOT cell is not possible.

The science cell has a better vacuum due to the pressure gradient established by a thin vacuum tube connecting the two vacuum cells. The tube between the MOT cell and the science cell allows a pressure gradient between the two cells, with the pressure in the science cell an order of magnitude less than the MOT cell. The vacuum in both cells is maintained by two ion pumps, and in the science cell an additional Titanium

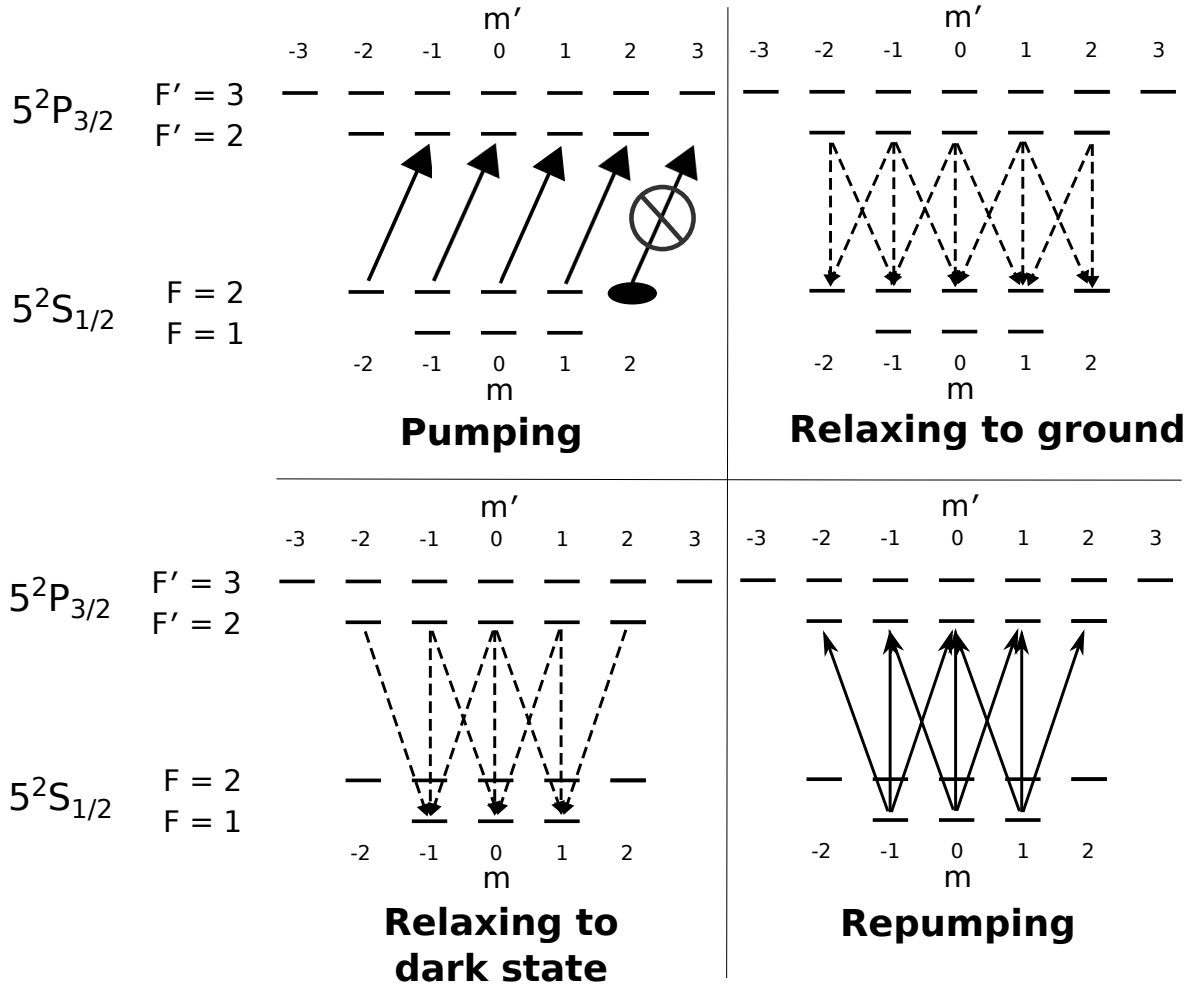

Figure 2.4: A diagram showing all the transitions involved in optical pumping. There are four possible transition types. **Optical pumping** is done by the pump laser beam. The pump beam is adjusted to have a σ^+ polarization at about 25 MHz red of the F = 2 to F′ = 2 transition. Due to the selected polarization's orientation with respected to the small bias magnetic field, the pump beam causes an atom to transition from the ground state to the pumped state with $m' = m + 1$. When excited up to the pumped state, the atoms can relax to either the F = 2 or F = 1 state. The atoms can **relax to the F = 2 state** with $m = m' \pm 1$ or with $m = m'$. Once in the ground state, the atoms continue interact with the pump beam. On the other hand, the atoms can also **relax to the F = 1 state** and be repumped by the **repump transition** similar to the process in MOT. Since all the transitions except the pumping transition randomly change the magnetic quantum number by ± 1 or leave it unaltered, while the pumping transition always increases the magnetic quantum number, after multiple cycles of transitions, most of the atoms arrive at the $m = 2$ substate of the ground state. Since the pumped state does not have an $m' = 3$ substate, once the atoms reach $m = 2$ substate after cycles of pumping, the atoms stop interacting with the pump beam. Except the atoms loss through background collsion, most atoms end up in this substate, depicted as an oval in the pumping diagram.

sublimation pump. The pressure in the MOT and science cell are typically in the mid 10^{-10} and 10^{-11} Torr respectively. The lower pressure in the science cell allows further reduction of the temperature of the atoms. The science cell contains the science trap that we use for our experiment. The science trap will be discussed in section Section 2.1.3. The science cell has six optical access ports, all of which are coated with anti-reflective coating to prevent unwanted scattered laser light. See Figure 2.1 for the diagram of the apparatus.

The atom cloud is moved to the science cell by a mechanical track upon which the spherical quadrupole coils are mounted. The track movement takes about 2 seconds to complete. The atoms are moved slowly enough for the process to be adiabatic.

Once the atoms have arrived in the science cell, we cool the atoms further using evaporative cooling. The depth of the trapping potential is reduced in steps. Each reduction allows the most energetic atoms to leave the trap. Between each reduction, the remaining atoms are allowed to rethermalize through elastic collisions. Since the atoms leaving the trap have energy higher than the average atoms, each depth reduction and rethermalization results in the atom cloud having lower average energy.

Eventually, the remaining atoms are cold enough that a significant portion of them can be ejected from the trap through a process called Majorana loss or a spin-flip loss [38]. Majorana loss happens when an atom passes through a region with no magnetic field. The atom losses its quantization axis allowing its magnetic moment to be misaligned with the magnetic field. In some cases, the misalignment puts the atom in an anti-trapping magnetic state. When the atom moves away from the field zero, it will be ejected from the trap. Thus, a trap with a field zero effectively has a hole for

atoms to escape through. There are multiple solutions to the problem [39]. We use a time-orbiting potential (TOP) trap. The basic principle of a TOP trap is the application of a rotating bias field that moves the zero-field position around the atoms. If the field rotates faster than the oscillatory frequency of the atoms in the trap, the atoms will experience an effectively static time-averaged potential from the rotating field. Since the atoms are in the low-field seeking state, they are trapped where the time-averaged field is minimum, which is at the center of the trap where the field is never zero. We assume that the frequency of the field rotation is much smaller than the Larmor frequency of the atoms, so that the spin of the atoms remains aligned with the magnetic field. A benefit of the TOP trap method is that the rotating atomic spins tend to cancel effects from extraneous stray magnetic fields that are not oscillating at the same frequency as the bias field [38].

Once the atoms are in the TOP trap, the nature of the measurement dictates the next steps. For some measurements, such as those in Section 3.2, we want the atom cloud to be as warm as possible, so that the atoms fill a large volume of the trap. We therefore cool the atoms to the highest temperature compatible with the final atom trap used. The right evaporation level is determined empirically to provide the greatest expanse in cloud size, while still giving a detectable signal.

Other measurements benefit from using a Bose-Einstein condensate, such as those in Section 2.3.2. In this case, we apply a second stage of evaporative cooling to reduce the temperature of the atoms further and to increase the phase space density, until reaching the transition to Bose-Einstein condensate (BEC).

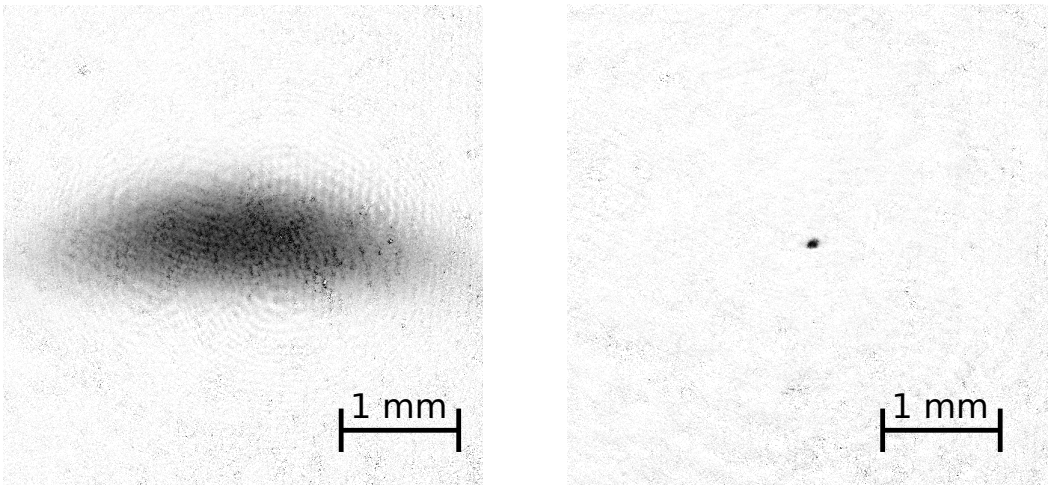

(a) Cold atom cloud **(b)** Bose-Einstein Condensate

Figure 2.5: Images showing a cold atom cloud and a Bose-Einstein condensate. Both images were captured using absorption imaging (see section 2.2.1 for the explanation of the technique). Both images were taken with the atoms in the science atom trap described in section 2.1.3

2.1.3 Science atom trap

While a tightly-confined spherical quadrupole trap was easily generated by two anti-Helmholtz coils, making some types of measurements in a tightly confined trap is counter-productive. For instance, in interferometry measurements, the further we can separate different atom packets, the easier and more accurate the measurement becomes. Furthermore, a tightly-confined trap results in greater interaction between the trapped atoms. Interatomic interactions destroy the coherence of the atomic wavefunctions and limits their interference. Implementing an atomic Foucault pendulum in a tight trap is also counter-productive. A weak trap permits larger oscillation amplitudes of the atoms, which facilitates detection of minute rotation of the oscillation plane. A weakly-confined atom trap, with gravity cancellation, is preferred for our measurements. For this purpose, we load the atoms into a "science trap".

The science trap uses a variation of the time-orbiting potential (TOP) method.

The trap's fields are generated by six coil chips, grouped as three pairs. Each coil consists of a strip of copper arranged in a spiral pattern on an Aluminum Nitride substrate. The chips were made using a photolithography technique. The chips are aligned to form a cube, with the two chips of a pair on the opposite sides. A CAD drawing of a chip can be seen in Figure 2.6. Each chip's current can be controlled independently. Drive circuits and control signal generation can be found in [6]. We denote the direction along the vacuum cell to be x, the other horizontal direction y, and the vertical direction z (see Figure 2.3). The x and y pairs are wired in series, while the two z chips are controlled independently.

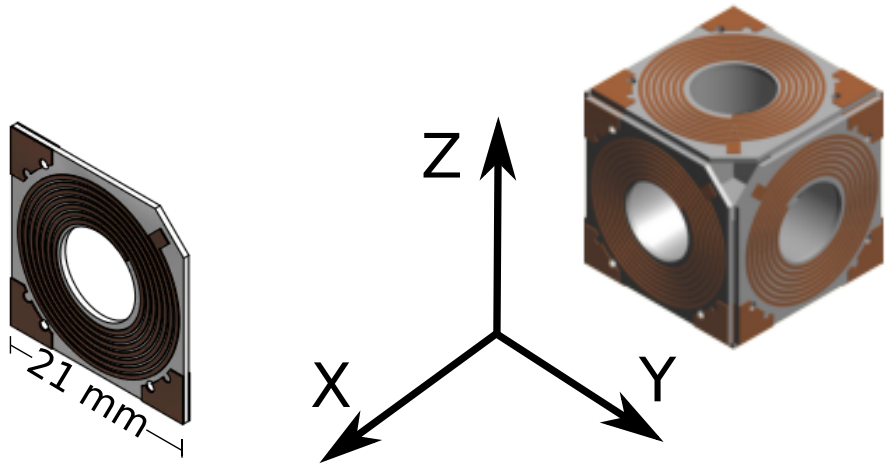

(a) A chip coil of the magnetic atom trap

(b) Magnetic atom trap cube

Figure 2.6: Diagrams showing a single chip coil. Six chip coils make up our magnetic atom trap. Diagrams from [6]

The currents fed to the coils generate two time-dependent magnetic fields: the bias field and the quadrupole field. The atoms are confined by the time-average of the

two fields. The two fields can be described, in lowest order, by

$$\vec{B}_{quad} = B_1' \cos\Omega_1 t \begin{pmatrix} x/2 \\ y/2 \\ -z \end{pmatrix} \tag{2.7}$$

$$\vec{B}_{bias} = B_0 \begin{pmatrix} \sin\Omega_1 t \cos\Omega_2 t \\ \sin\Omega_1 t \sin\Omega_2 t \\ \cos\Omega_1 t \end{pmatrix} \tag{2.8}$$

where B_1' is the quadrupole field amplitude, the value which will be determined to cancel gravitation potential energy (discussed later in this section), B_0 is the adjustable bias field amplitude, Ω_1 ($2\pi \times 10$ kHz) is the angular frequency of the quadrupole field, and Ω_2 ($2\pi \times 1$ kHz) is the angular freqency of the bias field.

The movement of the bias field can be understood as a superposition of two movements. First, it rotates around the origin in a circular motion on a plane containing the z-axis at frequency Ω_1. The second motion can be understood if we hold the $\Omega_1 t$ term constant and consider only the x and y terms. Here the field rotates about the z-axis at frequency Ω_2. For a diagram of the combined movement, see Figure 2.7.

Since both Ω_1 and Ω_2 are much faster than the oscillatory motion of the atoms in the trap (~1 Hz), but slower than the atom's Larmor precession rate (~10 MHz), the TOP trap as described successfully traps the atoms and avoids Majorana loss. The atoms only see the time-average potential caused by the time-average of the magnitude of the rotating field. In the lowest (harmonic) order, the time-average magnitude of the

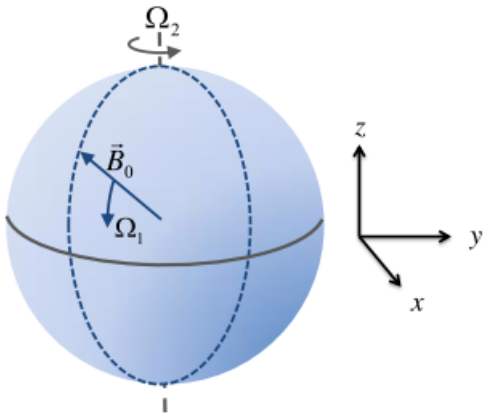

Figure 2.7: A diagram shows the movement of the bias field as a superposition of two motions. In the first motion, the bias field circles about the origin in the plane containing the z-axis. The second motion consists of the plane rotating about the z-axis. Diagram taken from [6].

rotating field can be found analytically:

$$|\vec{B}| = |\vec{B}_{bias} + \vec{B}_{quad}| \tag{2.9}$$

$$= B_0 \Bigg[1 + \frac{B_1'}{B_0} \sin\Omega_1 t \cos\Omega_1 t (x\cos\Omega_2 t + y \sin\Omega_2 t) \tag{2.10}$$
$$- 2\frac{B_1'}{B_0} z \cos^2\Omega_1 t + \left(\frac{B_1'}{B_0}\right)^2 \cos^2\Omega_1 t \left(\frac{x^2+y^2}{4} + z^2\right) \Bigg]^{1/2}$$

$$\langle|\vec{B}|\rangle \simeq B_0 \left(1 - \frac{1}{2}\frac{B_1'}{B_0} z + \frac{1}{128}\left(\frac{B_1'}{B_0}\right)^2 (7x^2 + 7y^2 + 8z^2)\right) \tag{2.11}$$

In the last step, we have expanded all the terms using Taylor expansions, kept only the second order terms, and performed a time-average of the magnetic field.

Knowing the time-average magnetic field, the potential seen by the atoms in $m_F = 2$ state can be described, together with the gravitational potential, as

$$U_{tot} = \mu_B B_0 + mgz - \frac{1}{2}\mu_B B_1' z + \frac{1}{2}m\omega_x^2 x^2 + \frac{1}{2}m\omega_y^2 y^2 + \frac{1}{2}m\omega_z^2 z^2 \tag{2.12}$$

With $B_1' = 2mg/\mu_B$, the gravitational potential can be cancelled by the term linear in z. Additionally, the constant first term can be ignored as it has no physical effects on the motion of the atoms. The time-average potential is then expressed as a 3D harmonic oscillator,

$$U_{tot} = \frac{1}{2}m\omega_x^2 x^2 + \frac{1}{2}m\omega_y^2 y^2 + \frac{1}{2}m\omega_z^2 z^2 \tag{2.13}$$

with

$$\omega_x = \omega_y = \left[\frac{2\mu_B}{m}\left(\frac{7}{128}\frac{B_1'^2}{B_0}\right)\right]^{1/2} \tag{2.14}$$

$$\omega_z = \left[\frac{2\mu_B}{m}\left(\frac{1}{16}\frac{B_1'^2}{B_0}\right)\right]^{1/2}. \tag{2.15}$$

Evidently, at the lowest order of approximation, the magnetic atom trap does exhibit cylindrical symmetry, one of the necessary conditions for a high-quality Foucault pendulum. However, even in this order, an accurate analysis should include the curvature of the bias field. Since our study measures these terms explicitly, and since any calculation with the curvature terms included is, at best, an approximation, we omit the treatment with curvature terms here. The readers who are interested in the derivation of the potential with curvature terms can consult [6]. The resulting potential with the curvature terms resembles Section 2.1.3, but the oscillating frequencies become

$$\omega_x = \omega_y = \left[\frac{2\mu_B}{m}\left(\frac{7}{128}\frac{B_1'^2}{B_0} - \frac{\gamma}{16}B_0\right)\right]^{1/2} \tag{2.16}$$

$$\omega_z = \left[\frac{2\mu_B}{m}\left(\frac{1}{16}\frac{B_1'^2}{B_0} + \frac{\gamma}{8}B_0\right)\right]^{1/2}. \tag{2.17}$$

2.2 Detecting the atoms

In this section, we will discuss the methods used to detect the trapped atoms. We use two detection techniques: absorption imaging and fluorescence imaging.

2.2.1 Absorption imaging

Absorption imaging provides a dark absorption profile on a bright, exposed background. A probe beam tuned to the transition as shown in Figure 1.5 illuminates the atoms and the surrounding area. The photons in the region around the atoms move through the space unobstructed. The photons in the region intercepted by the atoms are absorbed. The amount and the area of absorption depends on the density and the size of the atom cloud respectively. The shadow caused by the absorption can be analyzed to obtain the column density and the size of the atom cloud.

Once the probe beam has passed through the vacuum cell and the atoms, the photons impinging on CCD get converted linearly to a number of counts in each pixel based on the quantum efficiency of the camera. A system of lenses is used to image the atom plane onto the CCD (see Figure 2.8). Two cameras are used to provide 3D information. The system of lenses also magnifies the image. The lenses used for imaging are either achromatic lenses, which help in reducing spherical aberration, or microscope objective lenses. The magnification of the cameras (shown in Table 2.1) can be measured by deliberately moving the atoms in the spherical quadrupole trap a known distance by adjusting the mechanical track location, and correlating the physical shift with the shift in the image.

Camera	Magnification
Side Camera	1.58 ± 0.18
Top Camera	4.42 ± 0.01

Table 2.1: Table showing the magnification of the CCD cameras used in the experiment.

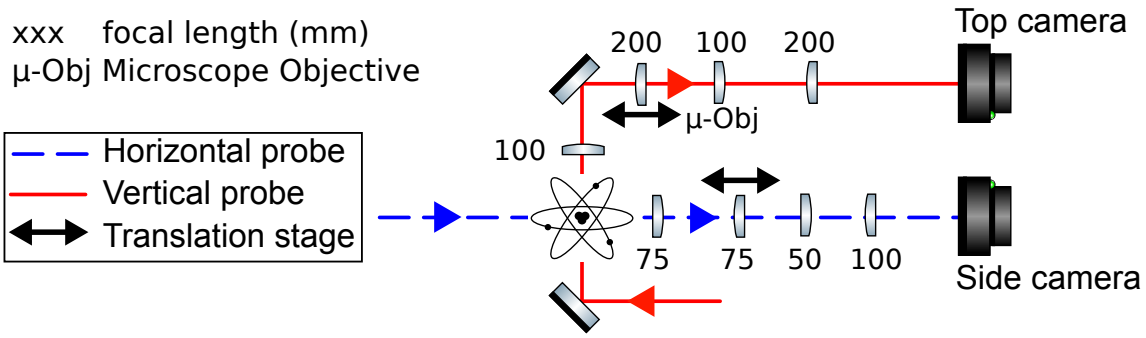

Figure 2.8: A schematic diagram showing laser and optics involved in absorption imaging. To get the best Gaussian profile, the probe beams are optical fiber launched. The two-sided arrows denote the lenses that are mounted on translation stages. The translation stages allow us to focus the atom cloud onto the cameras' CCDs. Two cameras allow us to study arbitrary motion in three-dimensional space. The CCD plane of the side camera runs parallel to the mechanical track and the length of the vacuum cells. The numbers next to the lenses indicate focal lengths. All the lenses are achromaic lenses, except the one microscope objective, Mitotuya M plan Apo 2x, which is marked accordingly on the diagram.

To understand absorption imaging quantitatively, the Beer-Lambert law can be used. When a probe light of intensity I_0 travels through atoms with absorption coefficient α, the intensity of the output light is

$$I_{\text{out}} = I_0 e^{-\int \alpha(z) dz} \tag{2.18}$$

where z is the direction along the probe beam, $\alpha(z)$ is the probability of a photon being absorbed per unit length at z. The probability of being absorbed is also related to the light scattering cross-section and the density of the absorbing atoms, $\alpha = \sigma n$ [40], where σ is the light scattering cross-section and n is the atomic density. Equation (2.18) and the relation between the cross-section and the probability of being ab-

sorbed are used to explain the absorption in our experiment:

$$I_{\text{out}}(x,y) = I_0(x,y)\exp\left[-\int \sigma(z)n(x,y,z)dz\right] \tag{2.19}$$

where (x, y) is the coordinate on the CCD camera, i.e. in the plane perpendicular to the probe beam's direction of travel.

The density distribution and the location of the trapped atoms can described by a mathematical model. Various models can be used for fitting. For most of our measurements, the use of a Gaussian density model works well. Since the potential is approximately harmonic, as shown in Equation (2.13), the Gaussian model is suitable for a cold atom cloud. For a BEC, the Thomas-Fermi approximation predicting an inverse parabola model is more accurate [41]. However, we find that using a Gaussian model for BEC is adequate in most cases. The 3D Gaussian model used is

$$n(x,y,z) = \exp\left[-a_1(x-x_0)^2 - a_2(y-y_0)^2 - a_z(z-z_0)^2\right] \tag{2.20}$$

where (x_0, y_0, z_0) is the location of the atom cloud's center. The a coefficients are the model parameters. In Chapter 3 when we try to measure the cloud profile to higher precisions, multiple higher-order terms will be added to the model.

Given the Gaussian model, the density distribution of the trapped atoms is a product of three independent density functions, each of which depends only on a single coordinate.

$$n(x,y,z) = n_x(x)n_y(y)n_z(z) \tag{2.21}$$

With the separation of variables, we can simplify Equation (2.19) by noting that the integration along z-direction can be evaluated independent of the x and y coordinates. Defining $B \equiv \int \sigma(z) n_z(z) dz$, we have

$$I_{\text{out}}(x, y) = I_0(x, y) \exp\left[-B n_{xy}(x, y)\right] \tag{2.22}$$

where $n_{xy} = \int n(x, y, z) dz$ is the column density through the location (x, y) in the xy plane. Since the number of counts on an image corresponds lineary to the intensity of the imaged photons, the intensity in the above equation can be replaced by the photon counts on the CCD without loss of generality.

Three images are taken for each absorption imaging measurement: the "atom" image, the "no-atom" image, and the "background" image. Each image has 80 μs exposure time. First, the background image is taken with the probe light off. Even when the best optical isolation techniques are used, completely eliminating unwanted scattered background laser light from being captured by the cameras is impossible. Since the unwanted background light is independent of the atom trap operation, images meant for measurements are corrected by subtracting the background image. Next, the "atom" image, an image of the atoms in the science trap is taken. The pixel counts of the atom image after background subtraction is represented by Equation (2.22). Lastly, the "no-atom" image is taken with the same optics and beam sequencing as the "atom" image but without the trapped atoms. Without any absorption from trapped atoms, the "no-atom" image provides a measurement of I_0.

After all three images are taken, the divided image can be calculated. For a pho-

ton count of $P(x, y)$ at the pixel (x, y) on the CCD, the same pixel value in the divided image is

$$\begin{aligned} P_{\text{divided}}(x, y) &= \frac{P_{\text{atoms}}(x, y) - P_{\text{bg}}(x, y)}{P_{\text{no atoms}}(x, y) - P_{\text{bg}}(x, y)} \\ &= \exp\left[-A - Bn(x, y)\right] \end{aligned} \tag{2.23}$$

where A accounts for small differences in overall probe intensity between the two images. The equation above shows that the pixel value in the divided image ranges from 1 to 0, depending on the column density of the atom being projected onto the pixel. An image representing the location-dependent density of the atom cloud can have an excellent contrast, as can be seen in Figure 2.5.

2.2.2 Fluorescence imaging

Fluorescence imaging provides an alternative way to detect the atoms. In contrary to the absorption images, fluorescence images provides a bright profile of atoms on a dark background. The same laser light we used for absorption imaging is also used for fluorescence imaging, but the beam is directed onto the atoms from the side, rather than into the camera. The illuminated atoms make a transition to the excited state upon photon absorption. When an atom decays through spontaneous emission to the ground state, it emits a photon in a random direction. When all the scattered photons are taken collectively, the atom cloud emit photons in all direction. The lens system images the atoms onto the camera's CCD. Since the photons are emitted in all directions, we can only collect the photons that are emitted in the direction of the first collecting

lens.

The number of photons generated at location (x, y) with is collected by the camera for an exposure interval t is

$$N_p(x, y) = \int n(\vec{r})dz \times A_{pixel} \times R_s t\mathcal{E} \tag{2.24}$$

where $n(\vec{r})$ is the density of the trapped atom at $\vec{r}$, A_{pixel} is the area in the object plane corresponding to one pixel on the camera's CCD sensor, R_s is the scattering rate as described in Equation (3.5), and $\mathcal{E}$ is the probability of an emitted photon to be collected by the lenses and detected by the CCD. Note that the photon count, not only depends on the atom density, but also depends on the duration of exposure, a property that is absent from absorption imaging.

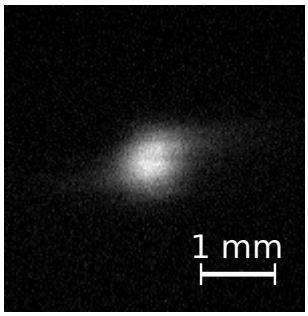

Figure 2.9: Fluorescence image of a cold atom cloud. The image is taken using the top camera exposed for 2 ms.

Note that the photon count in fluorescence imaging not only depends on the atom density, but also depends on the duration of exposure, a property that is absent from absorption imaging. Since the transition used for probing is not a closed transition, some atoms eventually find themselves in the F = 1 state. To avoid this, we apply repump light along with the probe. Two images are taken for a fluorescence measurement. An "atom" image is captured with trapped atoms present. A "no-atom" image is captured in the same condition but without the atoms. The difference between the two images yields the photon counts caused by the atoms.

2.2.3 When to use absorption or fluorescence imaging

In this section, we will discuss when and why we prefer one imaging technique over the other.

In general, absorption imaging provides a better image because it is independent of the probe beam intensity. This causes the absorption image to be more accurate. However, in some situations, fluorescence imaging is needed. The most obvious one is when the atom density is too small to produce enough absorption. For small absorption, absorption images are sensitive to noise in the background, which is always present at about 5% of fluctuation in the signal. Absorption imaging is not suitable for measurements that require a better sensitivity. On the other hand, since the photon count in fluorescence images is proportional to the product of atom density and exposure time, we can expose a fluorescence image longer to collect more photons when the atom density is insufficient for absorption imaging. Obtaining accurate photon counts for a given atomic density is difficult since it is hard to calibrate for variations in $\mathcal{E}$ and the probe beam density. However, for many purposes, relative measurements of density variation are adequate.

The ability to compensate for small atom density by increasing exposure is the main reason we have to use fluorescence imaging when we measure the potential profile's anharmonicity, the procedure which will be explained further in Chapter 3.

Regardless of the method used for detection, the trapping potential needs to be turned off. This is because atoms in a magnetic atom trap experience a significant Zeeman shift. For a large enough cloud, different parts of the cloud have different amounts

of energy shift. Since the scattering rate and the absorption rate depends on the detuning of the probe beam, the shape of the cloud is distorted by the difference in energy shift. It takes about 100 μs to turn off the trap, during which time the atoms move a negligible distance.

2.3 Inducing oscillation in the atom trap

In the last two sections, we have described the atoms that act as a bob for the atomic Foucault pendulum and the magnetic atom trap that provides the restoring force for the pendulum swing. First, we discuss how we set the pendulum in motion.

2.3.1 Kick coil

In classical Foucault pendulum, the pendulum motion is initiated by moving the bob away from the equilibrium, and then releasing it. We can achieve a similar effect in the atom trap by temporarily shifting the center of the trap adiabatically, to let the atoms be localized around the new center. The temporarily shift is achieved using an external magnetic coil, called the kick coil. Turning the kick coil abruptly off moves the trap center back to its original location. The displaced atoms then start to oscillate in the unshifted potential, analogous to the way a pendulum bob swings back and forth.

The amount and the direction of the trap shift depend on the orientation and the strength of the field generated by the kick coil. We can shift the center of oscillation by adding a field that is synchronized to the quadrupole field.

$$\vec{B}_{kick} = B_k \sin \Omega_1 t (a_x \hat{x} + a_y \hat{y} + a_z \hat{z}), \tag{2.25}$$

where B_k is the strength of the kick field and the a_i's are the direction cosines of the field, determined by the physical orientation of the coil. When the kick coil is active, the kick field adds simply to the quadrupole field:

$$\vec{B}_{quad+kick} = \frac{B_1' \cos\Omega_1 t}{2}\left[x - \frac{B_k a_x}{B_1'}, y - \frac{B_k a_y}{B_1'}, -2\left(z - \frac{B_k a_z}{2B_1'}\right)\right]. \tag{2.26}$$

Evidently, this is equivalent to the same quadrupole field, with the center now being shifted to

$$\left(\frac{B_k}{B_1'}a_x, \frac{B_k}{B_1'}a_y, \frac{B_k}{2B_1'}a_z\right). \tag{2.27}$$

The larger kick field we are able to produce, the larger the kick amplitude we can give to the atoms.

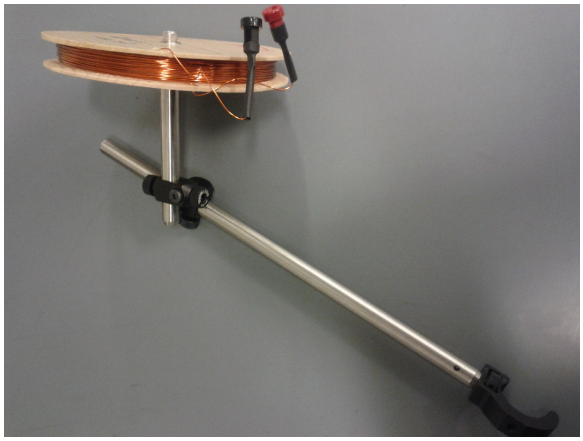

Figure 2.10: Kick coil and its mounting post.

A coil was wound with 22 AWG wire on a wooden frame. See Figure 2.10 for the assembled coil. The complete specifications of the kick coil is shown in table 2.2. The coil can be mounted to a standard 1/2" post. To easily align the coil in 3D and changing the direction cosines of the kick field, a swivel post clamp with 360° continuous-adjustability is used (Thorlabs, SWC). The whole structure is then mounted onto a post on the optics table using a C clamp on 1" post (Thorlabs, RM1C).

Properties	Values	Units
Number of turns (N)	25	turns
Diameter	15	cm
Inductance (L)	180	μH
Wire Gauge	22	AWG
Wire power rating	7	A
Maximum running current	5.7	A_{rms}

Table 2.2: Table showing specifications of the kick coil.

To run the coil, the signal used to drive the science trap's quadrupole field is split. One output is still fed to the audio amplifier for the science atom trap. The second output is connected to a phase shifter and an audio amplifier circuit in bridge-mono configuration (QSC audio products, LLC, RMX850). As stated earlier, we want the kick coil's current and the quadrupole field current to be in phase; the phase shifter allows us to correct for the electrical phase from the coil inductance and other elements. A current sense transformer (Triad Magnetics, CST306-2A) has also been installed inline to the kick coil to monitor the current through the coil. We choose the sense resistor to give a calibration of 1 V/A. The kick coil is turned on at the same time that the atom cloud is loaded into the science trap from the quadrupole trap. Once the atom cloud has situated in the science trap, the kick coil is turned off abruptly to induce an oscillation motion. An example oscillatory motion induced by the kick coil can be seen in Figure 2.12.

2.3.2 Bragg splitting

Rather than causing the atom cloud to oscillate as a whole, we can also split the cloud into multiple packets. In an ideal symmetric trap, if each packet is imparted with momenta that are different in magnitudes, but colinear in directions, their locations dur-

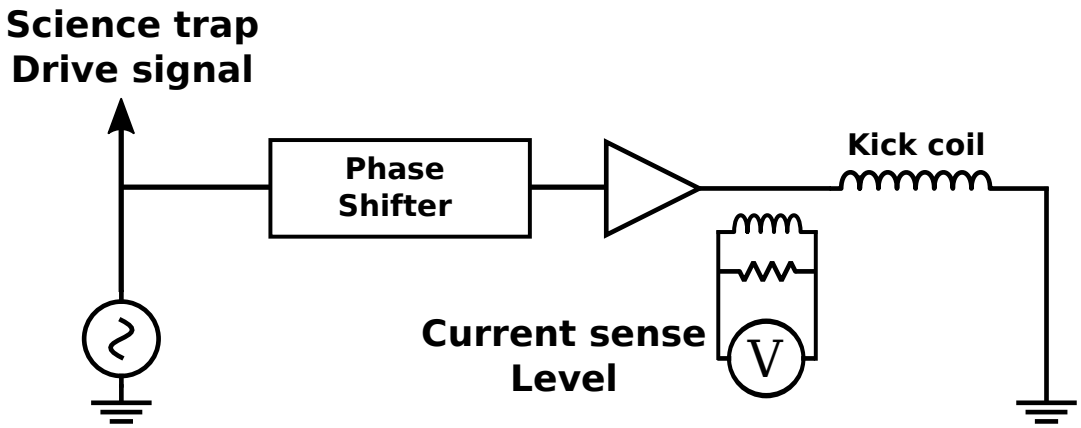

Figure 2.11: Circuit diagram of the kick coil

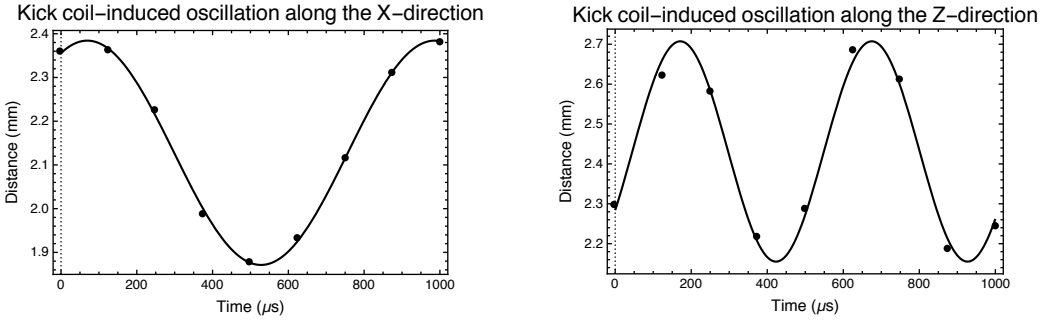

(a) Oscillation along the x-direction **(b)** Oscillation along the z-direction

Figure 2.12: Oscillation curves of the atoms in the science trap. The oscillation is induced by the kick coil. The atoms clearly show oscillatory motion in both directions shown. The second camera also takes pictures of the same motion from an orthogonal image plane. The images from both cameras allow us to map out the motion in three-dimensional space. The sinusoidal fits are provided as a guide to the eye. The period along the x-direction is about 900 ms, while that along the z-direction is about 500 ms.

ing oscillation will form a line. The line of oscillation is analogous to the line drawn in the sand by the bob in a classical Foucault pendulum. The orientation of the line will rotate due to the Foucault effect.

We use the optical Bragg scattering process to split the atom cloud. Two off-resonant laser beams create a standing wave at the atom location. In our case, one laser beam is retro-reflected. The presence of the standing wave creates a periodic

dipole potential for the atom [36]. The atoms scatter from this potential receive momentum transfer in discrete units of $2\hbar k$, where k is the wave number of the Bragg light. This optical Bragg scattering is complementary to crystalline Bragg scattering. In crystalline Bragg scattering, a periodic crystal forms a grating made of matter, from which light scatters. In optical Bragg scattering, atoms (matter) are scattered from an optical standing wave (light). In both cases, the amount of scattered momentum depends on the spatial period of the grating [42].

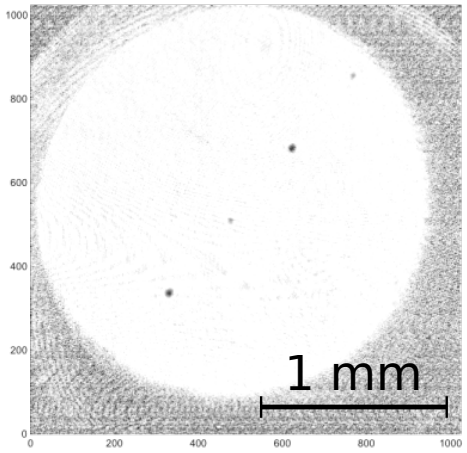

Figure 2.13: Bragg splitting of an atom packet

A Bragg scattering process also can be understood as a stimulated Raman transition. An atom absorbs a photon from one of the Bragg beam and makes a transition to an excited state. The absorption of the photon causes the atom to gain $\hbar k$ of momentum in the direction of the absorbed beam. The atom is then stimulated to emit a photon into the other Bragg beam, which travels in the opposite direction. This causes the atom to gain another $\hbar k$ of momentum. Overall, the entire process imparts $2\hbar k$ of momentum to the atom. By symmetry, the process is equally likely to occur with the stimulating beam and the absorbed beams' order reversed. In this way, the cloud of

atoms is split into two packets with $2\hbar k$ momentum gain but travelling in the opposite direction. A diagram depicting the process can be seen in Figure 2.14.

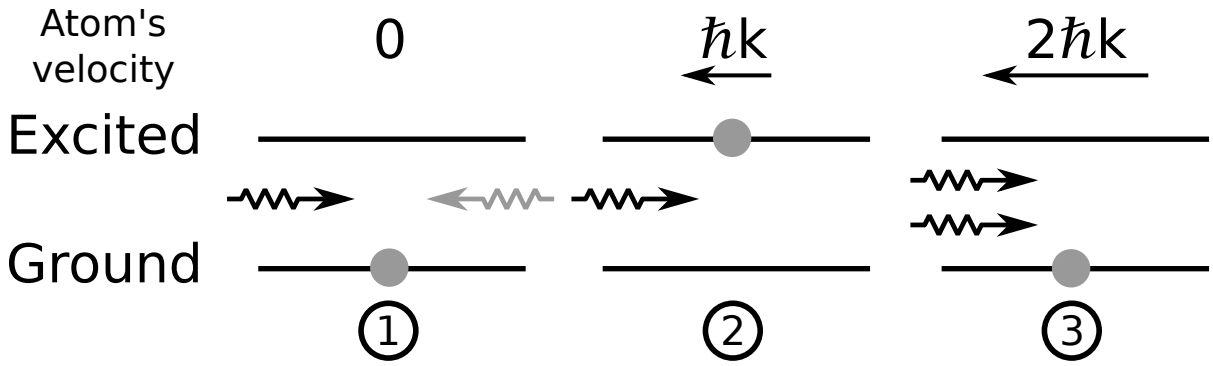

Figure 2.14: Diagram showing the process involved in Bragg splitting of an atom cloud in an ideal two-level system. The atoms starts at rest with light beams illuminating from both sides (Step 1). The atoms absorb the left-going photon and transitions to the excited state. Because of the absorption, the atoms gain $\hbar k$ momentum in the direction of the absorbed beam (Step 2). The atoms relax down to the ground state through stimulated emission by the other beam. Due to the emission, the atoms gain additional momentum, which brings the total momentum of the atoms to $2\hbar k$ (Step 3). By symmetry, the atoms is equally likely to start by absorbing the photon from the right-going beam. In the end, a single atom cloud is split into two identical clouds going in the opposite direction at the same speed.

As noted in Section 1.2, one of the difficulties for a classical pendulum is in the initial release of the pendulum. The initial velocity's problem in the classical Foucault pendulum becomes trivial to solve with Bragg scattering. If the potential profile is cylindrically symmetric, a Bragg scattering process in any direction in the horizontal plane guarantees a line of oscillation. No momentum is imparted on the atoms in the direction perpendicular to the Bragg beams.

Observing the oscillating atoms using Bragg scattering is easy to achieve, but it does have a siginificant constraint. Since the process imparts, at the minimum, a momentum of $2\hbar k$ on the atoms, it is impossible to study oscillation amplitudes smaller than $2\hbar k/m\omega$, where ω is the oscillation frequency on the same axis as the atom's velocity. When we need to vary the oscillation amplitude, we use the kick coil method instead.

Note that Bragg scattering is a widely-used phenomenon. In fact, many of our published results make use of the process [43, 44]. The Bragg splitting process discussed so far is limited to the first-order process. Higher order process are possible. In general, an nth-order Bragg splitting results in two atom packets moving in the opposite direction, each with a momentum of $2n\hbar k$. A modification also can be made such that asymmetrical splitting of atom clouds is possible [45, 46].

2.4 Trajectory analysis

We will discuss how we analyze the trajectory of the atoms in our atomic Foucault pendulum in this section. A suitable mathematical model is fit to the center position of the atom cloud. We use the same coordinate axes in analyzing the trajectory as the one we defined for the magnetic atom trap's notation (Figure 2.3). The motion along the x,y, or z axes are analyzed indepently. Since the leading order of the science trap's potential is a harmonic oscillator, each axis's motion is modeled by a simple sinusoidal function. The model for the j-axis is

$$j(t) = A_j \cos\left(\frac{2\pi}{T}(t + t_0)\right) + j_0 \tag{2.28}$$

where $j(t)$ is the location of the atom along the j-axis at time t, A_j is the amplitude of oscillation along the axis, T is the period of oscillation, t_0 is the phase offset of the motion, and j_0 is the center of the oscillation, generally representing the center of the trap.

2.5 Conclusions

In this chapter, our apparatus and techniques used are mentioned. How we plan on implementing a Foucault pendulum in the science trap was discussed. The analytical techniques used to study the atomic Foucault pendulum were described. In the next chapter, we will show the early results of our atomic Foucault pendulum. The early results show approximated cylindrical symmetry in our science trap. We will also discuss how the shape of the potential energy of the science trap can be studied in more details through the use of tomographic imaging.

3

Measuring the potential

The level of attention paid to the details in making a classical Foucault pendulum is a good example of how carefully tuned a Foucault pendulum has to be. In the last chapter, we presented our apparatus and discussed the techniques involved in analyzing the result. In this chapter, we will show that the science trap possesses approximate cylindrical symmetry. We will discuss why we need better symmetry to achieve a working atomic Foucault pendulum. The level of symmetry needed, as well as the effects from anharmonic terms will be discussed. Due to the level of accuracy needed for an atomic Foucault pendulum, we will implement a new

imaging technique allowing us to map out the shape of the potential energy in 3D up to the fourth-order dependence in spatial coordinates. The technique will be used in several measurements in this dissertation.

3.1 Initial results

In an ideally symmetric atom trap, both methods of oscillation inducing discussed in Section 2.3 should create a straight line trajectory for small duration observation. As the oscillation is observed for longer duration, the Foucault effect will come into play. Using Equation (1.4) and the location of our laboratory's longtitude location (38° 2' 16"N = 38.04°), we can estimate the rotation of the oscillation line, as a function of time, to be

$$T_{\text{Foucault}} = (24 \text{ hours})/\sin(38.04^\circ) = 38.95 \text{ hours} \tag{3.1}$$

In one minute, the line of oscillation will have rotated roughly 2.6 mrad. The Bragg kick amplitude is roughly 1 mm, so the rotation of the oscillation line corresponds to about 3 μm shift in the direction perpendicular to the trajectory. To detect such a small shift in distance, we increase the magnification of top camera to 12.3x from the normal value, as shown in Table 2.1, of 4.42x. This is equivalent to 512 pixels/mm. The increase in magnification can be trivially done by swapping out the microscope objective lens for another one with more magnification (See Figure 2.8 for optics elements involved in imaging). A 3 μm displacement in the science trap is equivalent to 1.5 px shift at the increased magnification. Our Bragg splitting operation has a standard deviation at roughly 0.7 px. For trapping durations longer than one minute, the loss due

to collisions with background gas causes a loss in atom signal. The lifetime of the atom cloud in the science trap is about 66 seconds.

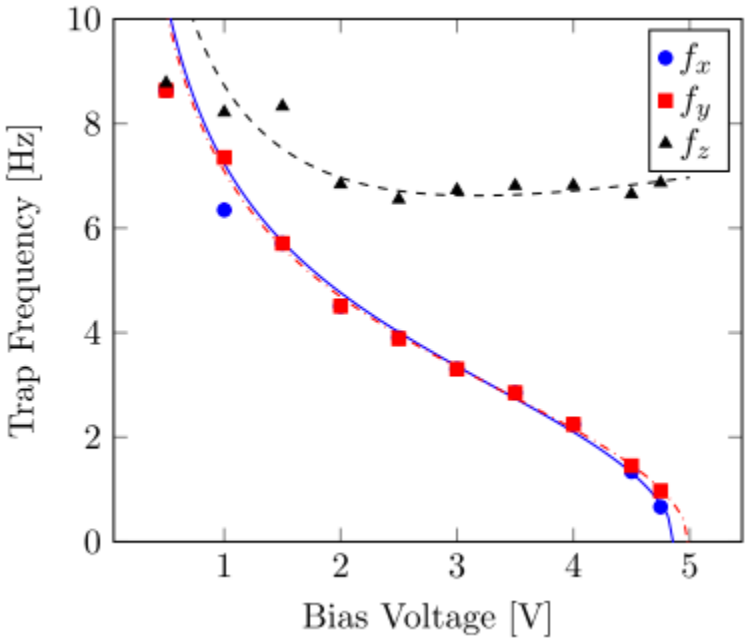

Figure 3.1: Robert Horne's oscillation frequency measurement. Diagram taken from [6]

Both Horne and I have independently verified the trap symmetry at the lowest order of approximation. In Horne's case, a Bragg-split atom cloud is made to oscillate in the magnetic atom trap. The frequencies of the oscillation were measured and shown in Figure 3.1. The oscillation frequencies in the x and y directions are identical, except at the higher limit of the bias field able to be generated by the magnetic atom trap.

Horne actually measured one period of oscillation, the amount of time typically need for an atom interferometry measurement. However, for an atomic Foucault pendulum, the oscillation lasts tens of seconds. To further investigate the cylindrical symmetry of the magnetic atom trap with more accuracy, the kick coil was used to set the atoms in motion. The bias field used corresponds to Horne's 4.5 V of bias voltage. The

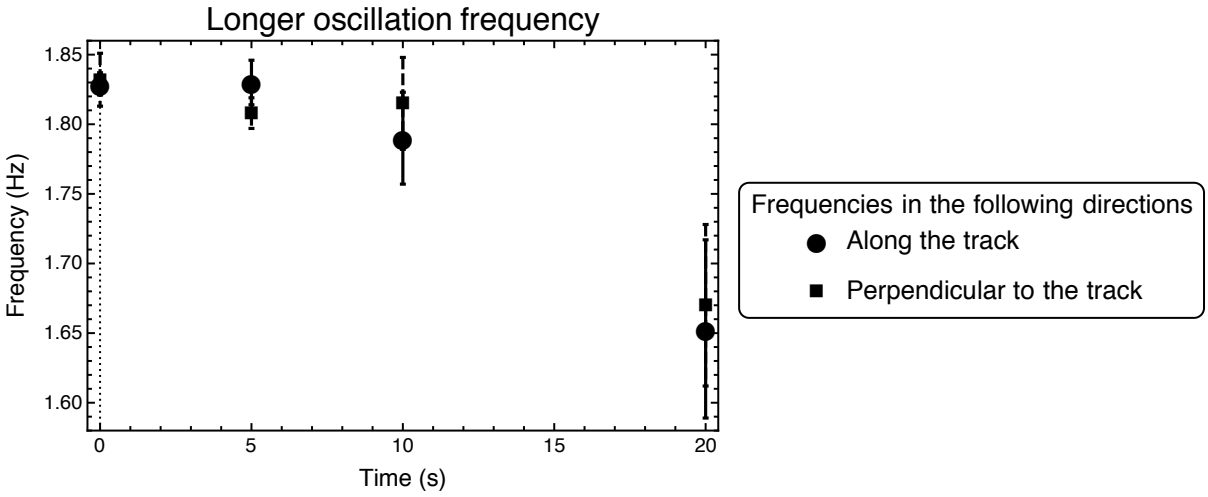

Figure 3.2: Initial measurement of oscillation frequency at long duration

trajectory data were taken after a set amount of time has elapsed since the atoms are kicked. The frequency of oscillation between the two horizontal directions agree within error for times up to 20 seconds (Figure 3.2). As can be seen, the average frequency does change slightly over time. This is due to thermal expansion of the trap structure as it heats up while operating. Fluctuations due to this effect eventually cause the atom oscillations to decohere, making the trajectory measurements impossible. This limits our observation time to about 20 seconds.

The effect of the thermal drift on an atomic Foucault pendulum is yet to be determined. However, if all the horizontal coils have the same thermal characteristics, a sensible assumption due to their identical construction and power load, the oscillation frequencies in the two horizontal directions should change together, thus preserving the symmetry needed for a Foucault pendulum. The technique developed in this dissertation will shed further light on this question.

3.2 Tomographic imaging

The result presented in the previous section is done by examining oscillations in the x and y directions. Since each data point takes roughly 3 minutes to measure, and each oscillation needs 8-10 data points, to measure the symmetry of a particular atom trap's setting takes about 1 - 1.5 hours. Analyzing trajectories for higher order components beyond the harmonic terms is also considerably more complicated, particularly in 2D or 3D. In this section, we will discuss tomographic imaging, a faster and more precise way to measure the potential profile of the atom trap.

Tomographic imaging refers to imaging in sections. The term was coined to describe medical imaging techniques, such as CAT scans, MRIs, and PET scans. Using methods that can image slices of the sample without actually cutting it, sections of the sample are obtained. The multiple sections can be compiled together to produce a three dimensional model of the sample, including internal structure, without ever having to cut the sample open [47].

A trapped atom cloud is the tomographic sample in our measurements. The density distribution of the cloud is related to the trapping potential through the equation

$$n(\vec{r}) = n_0 \mathrm{e}^{-\frac{U(\vec{r})}{k_B T}}, \tag{3.2}$$

where k_B is the Boltzmann constant, T is the temperature of the cloud, and n_0 is the peak density of the cloud. Both absorption and fluorescence imaging (Section 2.2) provide two 2D projections images per measurement. While, in theory, a 3D reconstruc-

tion of the atom cloud is possible from two 2D projections, a tomographic method can provide a more accurate and efficient way to measure the 3D distribution of the atoms, a quantity needed to fully characterize the magnetic atom trap. With a complete 3D reconstruction of the atom cloud and the relation of Equation (3.2), we can determine $U(\vec{r})$. In order to create tomographic images, we need to be able to selectively detect, i.e. sectioning, only a certain part of the atom cloud.

There are three major steps in acquiring tomographic images of the cloud. We provide a brief overview in this paragraph, with a detailed explanation to follow. First, the atoms are released from the science trap. Then, we make all the atoms transparent to the probe beam by transfering them into the F = 1 state by applying a pumping beam. Next, a two-dimensional slice of the cloud is reactivated by repumping the desired slice back up into the F = 2 state using the repump laser with modified beam shape. In our case, we shape the repump light into a light sheet using a cylindrical lens. Lastly, the probe light illuminates the entire cloud. Since most of the atoms are not reactivated, the fluorescence photons come solely from the active region of the cloud. Moving the repump sheet around allows us to image different slices of the cloud. A combined image can then be created from all the slices to present a three-dimensional picture.

While absorption imaging has been our main method in detecting Bose-Einstein condensate clouds, it is inadequate here. Only a small portion of the atom cloud is used to create tomographic images. As discussed in Section 2.2.3, absorption imaging does not work quite as well as fluorescence imaging for detecting low density atom clouds, especially in the regime in which the amount of photon absorption by the atoms

is on the same level as the probe background noise. A thin slice of an atom cloud absorbs too few photons to be of any practical value in tomographic imaging. At the thickness used in our tomography, the contrast in an absorption image would be reduced by 95%. For this reason, fluorescence imaging is preferred.

As mentioned in the previous chapters, the trapped atoms are in the F = 2, m = 2 state. To initiate the tomographic process, the science trap is turned off. At the same time, pump light tuned to the F = 2 to F′ = 2 transition is applied to the atoms (Figure 1.5). Since no repump light is applied during this stage, after sufficient amount of time, all of the atoms in the cloud will decay into the F = 1 state after a few absorption/emission cycles. Note that the pump light used in this step is the same light that was used to prepare the atoms for magnetic trapping (Section 2.1.2). The intensity of the pump light is 3.3 mW/cm^2, and we apply it for 30 μs. We can verify that all the atoms are in the dark state by looking at fluorescence images with and without the pump beam. With the pump beam applied, the fluorescence image is indistinguishable from the no-atom (background) image.

After all the atoms are in the dark state, we reactivate a slice of the atom cloud by shining repump light onto the region. The repump light used in this stage is tuned to the same F = 1 to F′ = 2 transition used for the MOT. The atoms illuminated by the repump beam are optically pumped back to the F = 2 state.

Since 2D slices of the cloud are desired, we have to shape the repump beam to suit our purposes. First, we launch the beam through a single-mode optical fiber to clean up the spatial mode of the beam. The resulting beam has a clean Gaussian profile. The repump beam then goes through a set of optics to reshape it into a light sheet.

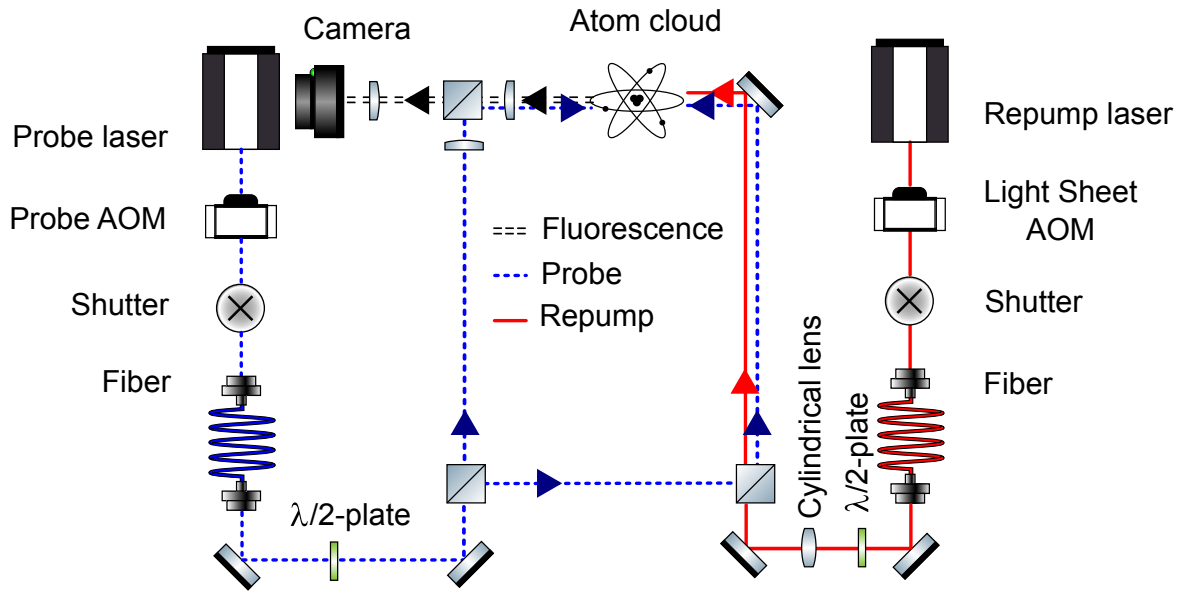

Figure 3.3: Schematic diagram of fluorescence imaging optics. Pump light is omitted from the diagram. Both of the laser beams can be triggered on/off through a combination of an acousto-optic modulator and a shutter. Both lasers were fiber launched to clean up the beam profile. Various $\lambda/2$-plates are installed to adjust the direction of the beams through the polarizing beamsplitters. The repump light has a cylindrical lens to shape the beam into a light sheet. The focal length of the cylindrical lens is selected such that the focal point of the light sheet is on the atoms. The probe beam is split into two beams to create optical molasses on the atoms to preserve the shape of the cloud during imaging.

The most crucial element is a cylindrical lens with a one-meter focal length. The cylindrical lens focuses the beam in only one dimension. This produces a sheet-like, 168 μm thick laser beam that is sent to the atoms. By rotating the cylindrical lens, the orientation of the sheet can also be changed. We normally run the sheet horizontally due to the fact that our Foucault pendulum will oscillate in a horizontal plane.

After the repump beam has been shaped, it is merged with the probe beam through a polarizing beamsplitting cube. The repump intensity at the atom is about 8 mW/mm^2. To obtain a fluorescence image, both the probe beam and the repump beam simultaneously illuminate and reactivate a selected horizontal slice of the whole atom cloud. The emitted fluorescence photons from the reactivated atoms are collected by an Apogee

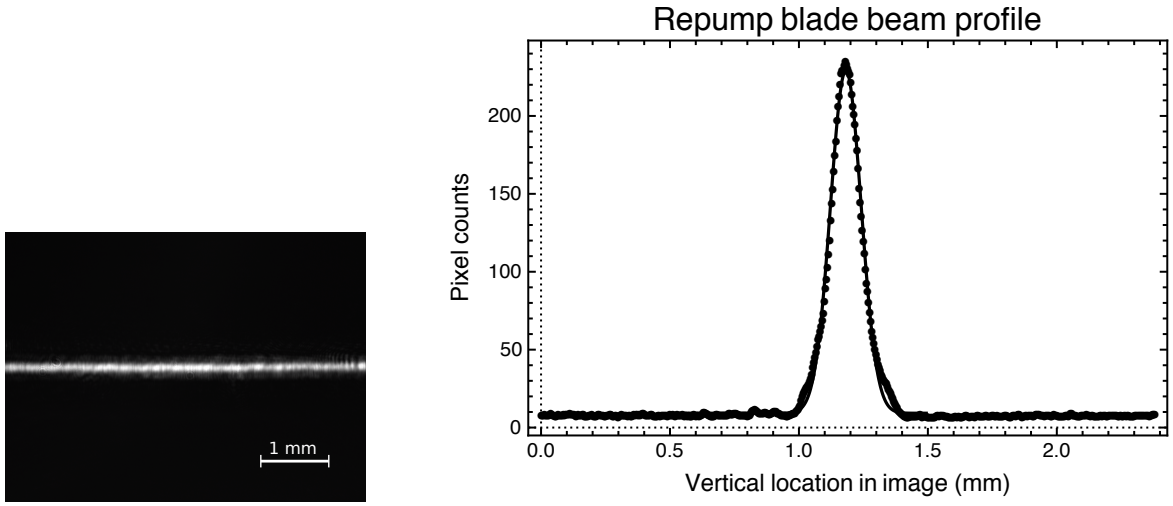

(a) Repump light sheet on the camera

(b) Repump light sheet profile

Figure 3.4: The profile of the repump light sheet as seen on the side camera and the Gaussian fit of the cross-sectional profile. The Gaussian model of the blade beam is seen in Figure 3.4b. The model can be described by $229 \exp -\frac{(x-1.18)^2}{0.084^2} + 9.2$. This gives the $1/e^2$ diameter of the light sheet along the thin direction as 168 μm.

U6 camera located right above the science trap. A single fluorescence image consists of about 30000 collected photons.

It is important to ensure that the measurement process does not alter the density distribution. The probe light exerts radiation pressure on the atoms, which causes the atoms to move, and could lead to an inaccurate result. We take several measures to avoid this effect, which are presented here.

First, two counter-propagating probe beams create an optical molasses on the atoms. If we only probe the atoms from one direction, the whole cloud will be pushed along the direction of the probe beam. Since our probe intensity is well over the saturation intensity, the acceleration on an atom due to radiation pressure of one probe beam is

$$a = \frac{F}{m} = \frac{\hbar k}{m}\frac{\Gamma}{2} = \frac{v_r}{2\tau}, \tag{3.3}$$

where τ is the lifetime of the excited state, 26.2 ns and v_r is the recoil velocity, 5.8845 mm/s [48]. Using these known values, we calculate the displacement of the atoms experiencing only one probe beam to be 1.26 mm for a probe beam duration of 150 μs. Considering that a typical cloud's diameter is about 1 mm, without a method to prevent this effect, the image would show a distorted superposition of the cloud locations over the probe time. Moreover, as the atoms are pushed, they gain velocity, which leads to a significant doppler shift and corresponding change in scattering rate.

Instead, we split the probe beam into two counter-propagating beams as shown in Figure 3.3. The two beams are slightly red-detuned by 3.9 MHz from the transition. The resulting optical cooling effect prevents the atom velocity from growing too large. Note that the smaller the detuning, the more photons we can collect, if the atoms still remain in the probing area. The optimal value for the detuning was determined empirically by maximizing the fluorescence signal after 2 ms of exposure time. This test duration is arbitrarily picked to be much longer than the actual probe duration. Any failures in arranging for effective optical molasses are amplified at longer time scale. The fact that the detuned light generates a larger signal than resonant light confirms the effectiveness of the optical molasses. In a similar manner, we optimize the power balance between the two beams. Figure 3.5 show profiles of the atom cloud at the optimized detuning, but various beam-power balance. A well-balanced beam power should maintain the Gaussian shape of the atom cloud due to equal radiation pressures from both sides.

Second, even with a well-balanced probe beams and carefully-adjusted detuning, the shape of the cloud still changes slightly if the probe beams are applied long

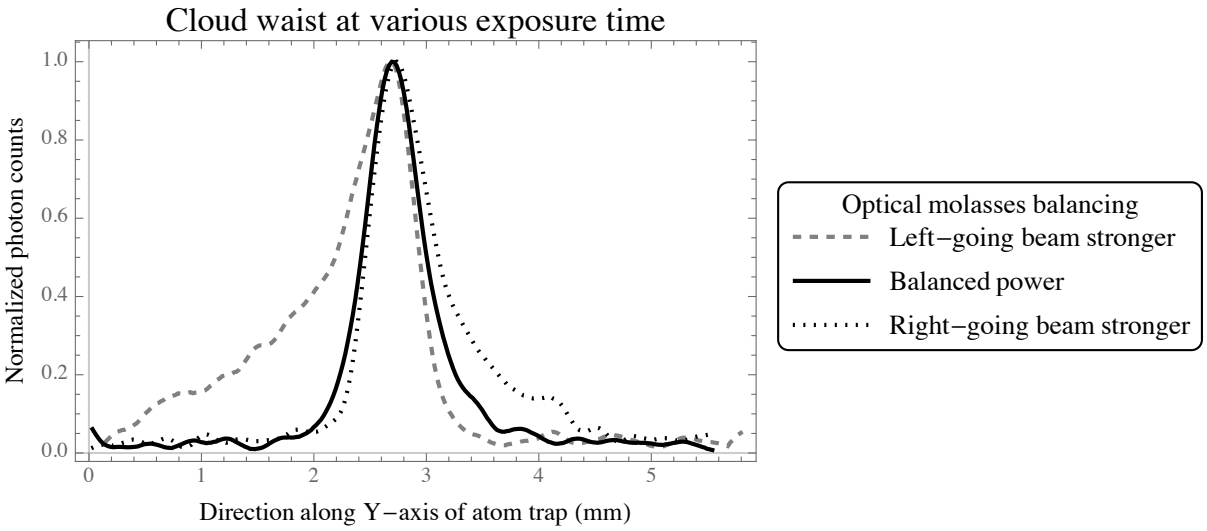

Figure 3.5: Atom cloud's profiles at various probe beam balance. When the power between the two probe beams is not balanced, exposing the atom cloud for 2 ms results in the cloud skewing in the propagating direction of the stronger beam. With well-balanced power, the atom cloud's cross section profile regains its symmetric shape. The images had a Gaussian filter with a radius comparable to that of the repump sheet width applied to smooth out the noise in the probe beam intensity.

enough. The choice of exposure time involves a tradeoff between increasing the signal to noise ratio of the image and disturbing the shape of the atom cloud. The longer the exposure time, the more counts we can get from the same atom cloud. However, longer exposure time leads to increase in radiation pressure effects. In order to find the optimal exposure time, we expose the atom cloud at various durations. The width of the atom cloud along the direction of the probe beams can be plotted as a function of the exposure time. From Figure 3.6, we can see that the cloud waist increases due to radiation pressure. The size of the cloud between 75 μs and 250 μs is the same within one standard deviation. The increase in the cloud size becomes statistically significance around 300 μs. To ensure minimum disturbance on the cloud's shape, we choose to expose our images at 150 μs. This gives as large a signal as possible, while still retaining the shape of the cloud.

A third issue is that the atom cloud, after being released from the trap but before

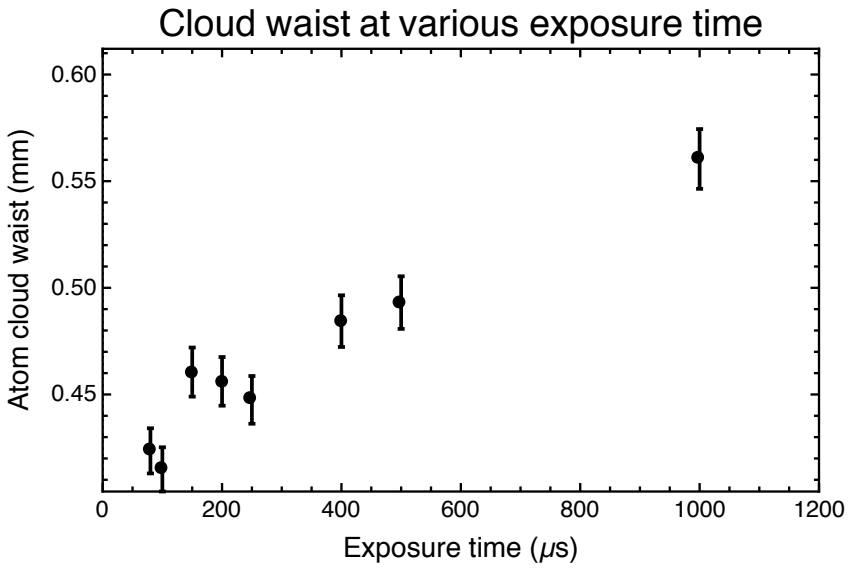

Figure 3.6: We chose to expose our images at 150 ms. At this exposure duration, the atom cloud's waist has not expanded significantly from its original value. The data was taken at the typical detuning of the probe beam of -3.9 MHz.

being probed, expands due to its non-negligible temperature. This leads to distortion of the cloud shape. To minimize this effect, we use the shortest possible delay between the releasing of the atom cloud and the probing of it. We can estimate the amount of expansion undergone by the atom cloud by using the temperature measured in Section 3.4 and the delay duration as shown in Table 3.1. From equipartition theorem, an ideal gas cloud at temperature T will have the mean squared velocity in one dimension [49]

$$\frac{1}{2}k_B T = \frac{1}{2}m\langle v^2\rangle, \tag{3.4}$$

where k_B is the Boltzmann constant and m is the mass of a Rubidium atom. Substituting the values for the constants, we find that, given the calculated root-mean-square velocity, the atoms travel about 2 μm during the delay. Given the typical width of the atom cloud of 2 mm, the increase of 2 μm to the atom's width is negligible.

A fourth issue is that, with our minimally perturbative probe, the fluorescence sig-

Accumulated time (μs)	Step duration (μs)	Actions
0	110	Waveguide turned off
110	30	Pump beam applied
140	5	Shutters operation
145	150	Probe and repump beam applied

Table 3.1: Table showing the duration of each step in probing the atom cloud for fluorescence imaging

nal is weak. The amount of estimated photons hitting a single pixel from a slice of the atom cloud is roughly 50 counts. Compared to the background noise of approximately 30 counts, the signal is barely larger than the noise. We address this by grouping pixels of the camera together to obtain better signal. When a photon emitted by the atoms strike a pixel on the camera's CCD, there is a probability, which is determined by the quantum efficiency of the camera that a count is registered on the image. We can increase the camera's sensitivity by grouping multiple pixels together. For all of our images, the pixels are either grouped in 6x6 arrays or 8x8 arrays. The photon counts in any of the pixels in the same array are summed together to provide a brighter composite pixel. This reduces the resolution of the image. An individual pixel is 5.4 μm x 5.4 μm at the object plane. For a 6x6 and 8x8 grouping, the pixel becomes a square with the side length of 32.4 μm and 43.2 μm at the object plane, respectively. However, the overall shape is unaltered by the binning. We can bin up the pixels of the CCD to the limit imposed by the cameras. The binned pixels are still much smaller than the atom cloud's extent.

Due to a low signal-to-noise ratio of a single fluorescence image, for a particular trap configuration, we typically take multiple images and use the average image to obtain the fit parameters of the atom cloud. A single image has a signal-to-noise ratio of

around 2, whereas an average of 100 images can provide a signal-to-noise ratio of about 60.

A final source of error is spatial variation in the probe beam intensity, which could appear as atom density variation. While the number of photons scattered by the atoms has the same profile as the density profile of the atom cloud, it also depends on the intensity and the detuning of the probe beam according to the equation [29]

$$R_s = \frac{\Gamma}{2}\left(\frac{I/I_s}{1 + I/I_s + 4\Delta^2/\Gamma^2}\right), \tag{3.5}$$

where R_s is the scattering rate, Δ is the detuning, Γ is the natural linewidth of the transition, I and I_s are the intensity of the probe beam and the saturation intensity of the transition respectively. If the scattering rate is lower at some location because of the lower intensity, then the region will appear to have fewer atoms. At our probe detuning and probe beam intensity, I/I_s is 8.83, while $4\Delta^2/\Gamma^2 = 1$. the term depending on the detuning is negligible compared to the I/I_s term. For light intensity much larger than the saturation intensity, the scattering rate becomes a constant, $\Gamma/2$. The probe beam power is made much brighter than the saturation intensity of the probe transition because of the constant scattering rate. With both probe beams together, the combined intensity is 31.6 mW/cm^2, compared to the saturation intensity of 3.58 mW/cm^2. Due to the constant scattering rate, any variations in the probe light power over the region of the atom cloud has no detectable effects on the cloud's shape.

We have also verified this empirically by intentionally lowering the overall probe beam intensity and comparing the resulting images. The range intensity variation found

in our probe beam is about 10%. The range of the overall intensity variation in this test is 30%. We find no statistical difference between the images taken with varying probe beam power.

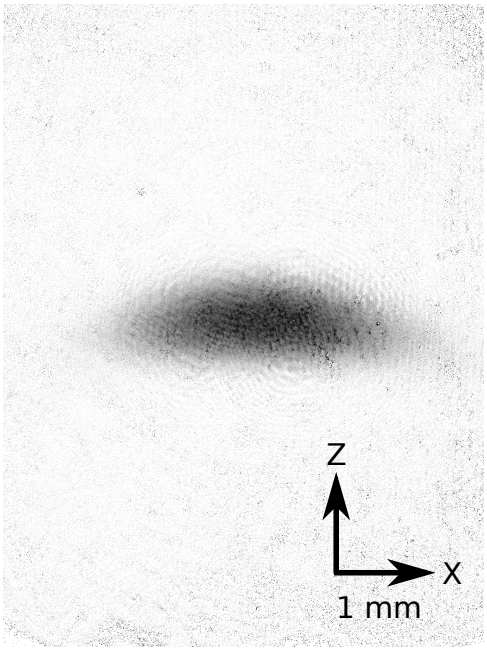

(a) Absorption image of the full cloud on the side camera

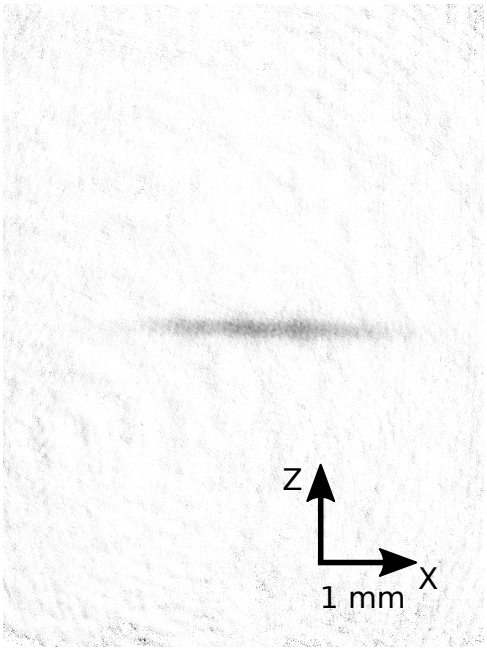

(b) Image using light sheet

Figure 3.7: Figures showing an application of the tomographic imaging method. Absorption images from the side camera are shown to illustrate the profile of the sectioned cloud. For density measurement, we use fluorescence imaging on the top camera. The distorted shape seen in Figure 3.7a is due to the anharmonicity of the trap. A full treatment of the topic will be discussed in Chapter 5.

3.3 Analyzing the atom cloud

To investigate the harmonic and higher-order terms of the potential, we describe the atom cloud profile in a power series according to the following equation

$$n(\vec{r}) = n_0 \exp[-P(x, y, z)] \tag{3.6}$$

where $P(x, y, z)$ is a polynomial describing the density distribution of the atom cloud. Since our slice is always performed at a fixed vertical height, fixed z, and since a constant term in the exponent is reflected in the constant coefficient, we can simplify the polynomial to have only x and y dependence.

$$\begin{aligned} P(x,y) =& a_{xx}x^2 + a_{yy}y^2 + a_{xy}xy \\ &+ b_{xxx}x^3 + b_{yyy}y^3 + b_{xyy}xy^2 + b_{xxy}x^2y \\ &+ c_{xxxx}x^4 + c_{yyyy}y^4 + c_{xxyy}x^2y^2 + c_{xyyy}xy^3 + c_{xxxy}x^3y \end{aligned} \tag{3.7}$$

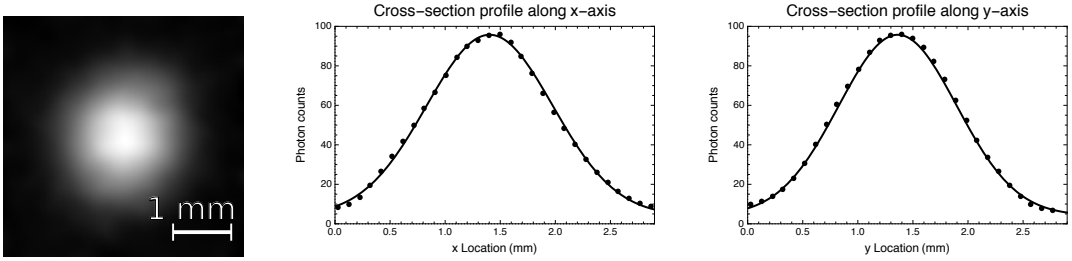

(a) Fluorescence average image of an atom cloud

(b) Cross section along x-axis

(c) Cross section along y-axis

Figure 3.8: The atom cloud shown in Figure 3.8a is fitted to the model described in Equation (3.7). The model provided a good description of the atom cloud as can be seen in the comparison of the cloud's profile and the fitted function. One hundred single images were averaged together to provide one average image. The atom cloud was taken at $z = 0$. The fit results and errors are shown in Table 5.1.

Due to thermal motion of the trap structure, the cloud location can shift from shot to shot. To obtain an accurate average image, we fit each individual image to a simple Gaussian to find the center of the cloud. Each image from a measurement set is then shifted to have their centers aligned before the average. With the average images, we can create a statistically more accurate profile of the waveguide.

The atom cloud images are fit using the least-square method. The error from the

fit is estimated by varying each fit parameter such that the χ^2 is doubled. χ^2 is defined as

$$\chi^2 = \sum_{i=1}^{N_p} \frac{(f(i) - c(i))^2}{\sigma^2} = \sum_{i=1}^{N_p} N_{avg} \frac{(f(i) - c(i))^2}{c(i)} \tag{3.8}$$

where N_p is the total number of pixels, $f(i)$ is the photon counts for the i-th pixel according to the mathematical fit, $c(i)$ is the actual photon counts for the same pixel, N_{avg} is the number of single images used to create one average image. The noise in the image is assumed to follow a Poisson distribution, i.e. $\sigma^2(i) = \sum c(i)/N_{avg}$. The reduced χ^2 determines how good the fit is and is defined as $\chi^2/(N_p - j)$, where j is the total number of parameters used in fitting. Reduced χ^2 having its value close to one signifies a good fit of the model [50]. An example of an image fit can be seen in Figure 3.8. For the image showed, the fit results and corresponding errors can be found in Table 5.1. The reduced χ^2 of the fit is 0.74.

3.4 Temperature measurement

While most of the interesting quantitites can be measured through the tomographic images, from Equation (3.2), we need to know the temperature of the atom cloud in order to make any meaningful comparison and calculate the potential of the trap. As described in Section 3.3, the potential of the trap can be expanded as a power series in x and y, where the two axes are defined as in Figure 2.3. A small enough kick along one of the principal axes should significantly reduce the effect of the higher-order terms on the oscillation frequency.

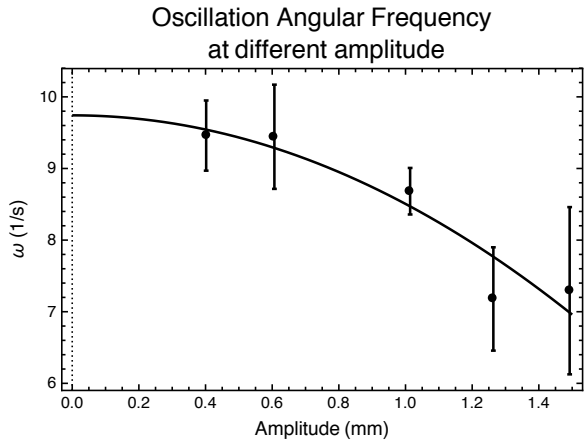

Figure 3.9: A plot showing the angular frequency of the oscillation induced by the kick coil. Oscillation smaller than 0.4 mm amplitude has large error bars due to atom trap loading fluctuation. We omit those data points from the plot. A parabolic fit of the data is provided. At small amplitude, the angular frequency asymptotically approaches 9.74 s^{-1}.

To find the cloud's temperature, we separately measure the angular frequency at small amplitude. We need to be able to control the oscillation's amplitude to lessen the effect of the higher order terms. Since the error in measuring the anharmonic terms is about 5%, it is reasonable to minimize the effect of the higher order terms to be less than the error. Given the magnitude of the anharmonic terms, an oscillation smaller than about 0.5 mm is adequate. To isolate the harmonic term in the potential, we use the kick coil, as described in Section 2.3.1, for a continuously-adjustable amplitude of the oscillation. With the kick coil, the amplitude can be made arbitrarily small. We measure the oscillation frequency along a particular direction that is convenient for the kick coil installation, the $x = y$ line, as a function of the oscillation amplitude. The results are shown in Figure 3.9.

The change in the oscillation frequency is minimal for the two smallest amplitudes, in agreement with our earlier estimation that an oscillation with an amplitude smaller than 0.56 mm should see no observable effect from anharmonicity. A parabolic fit is used to extrapolate to infinitesimally small amplitude. The oscillation frequency asymptotically approaches $\omega = 1.55(0.06)$ s^{-1} as the oscillation amplitude decreases.

From the atom cloud profile equation used in fitting the atom cloud images (see Section 3.3), we can find the harmonic term along the same axis and compare it to the

oscillation period measured here. With the atom trap at the harmonically symmetrical setting (see Section 4.2), we measure the harmonic term along the same axis as the kick axis to be $a_1 = 1.6(1)$ mm^{-2}. Comparing the atom cloud profile equation Equation (3.6) to the Equation (4.1), we can calculate the temperature of the atom cloud using

$$a_1 = \frac{\frac{1}{2}m\omega^2}{k_B T} \tag{3.9}$$

Substituting the measured numbers and constants into the equation above results in the temperature of the cloud $T = 300.51 \pm 24.2$ nK.

3.5 Conclusions

We have shown the early results of approximated cylindrical symmetry obtained through oscillation measurement. We have described the need for tomographic imaging in measuring the symmetry of the trapping potential, and how the technique will be an improvement over oscillation measurement. The apparatus and methods for tomographic imaging were discussed. The mathematical model used to describe the trapping potential up to the anharmonic terms is proposed. In the next chapter, armed with tools to perform tomographic imaging, we will explain how the harmonic terms are measured and adjusted for symmetry.

4

Harmonic terms

Chapter 3 showed that our trap provides a reasonable degree of symmetry, but we focus now on this question in detail. In particular, we consider the requirements for the harmonic terms in the potential. While the potential of the magnetic atom trap shown in Equation (2.13) exhibits cylindrical symmetry, our measurements indicate that there is residual asymmetry in the actual potential. Further fine-tuning is needed to make the trap more perfectly symmetric. We will show theoretically that the science trap can be tuned to achieve cylindrical symmetry, at least in the harmonic terms. Empirical evidence supporting the claim will be presented. Lastly, we

will discuss the maximum-acceptable level of harmonic asymmetry allowed for atomic Foucault pendulum.

4.1 Asymmetry in harmonic terms

While the potential of the magnetic atom trap shown in Equation (2.13) suggests cylindrical symmetry, the real potential is different and might not be cylindrically symmetric. There are many possible clauses including imperfection in the coil chip fabrication and assembling, extraneous magnetic fields from current leads, or inaccuracy in the drive currents. We can describe the potential more precisely by examining its Taylor's expansion. For a fixed vertical height z, if we expand the potential up to terms of second order in the coordinates, we have

$$U(x,y) = k_B T(a_{xx}x^2 + a_{yy}y^2 + a_{xy}xy), \quad \text{at fixed z} \tag{4.1}$$

$$= k_B T \begin{pmatrix} x & y \end{pmatrix} \begin{pmatrix} a_{xx} & a_{xy}/2 \\ a_{xy}/2 & a_{yy} \end{pmatrix} \begin{pmatrix} x \\ y \end{pmatrix} \tag{4.2}$$

where k_B is the Boltzmann constant and T is the temperature of the atom cloud. The coefficient $k_B T$ is introduced to be consistent with Equation (3.7). The assumption of fixed vertical height reflects fact that proposed motion will be mainly in the xy plane.

To analyze the potential, the matrix form of the potential as used in Equation (4.2) is the most convenient. We can classify the terms in the potential into two categories: the diagonal terms (a_{xx} and a_{yy}), and the cross terms ($a_{xy}/2$). For a perfect Foucault pendulum, the diagonal terms are equal, and the cross terms are zero. The resulting

potential is clearly cylindrically symmetric. Additionally, two out of three major factors (asymmetry and initial velocity problem) affecting the quality of a Foucault pendulum outlined in Section 1.2 are immediately optimized. There is no asymmetry because x and y are interchangable without changing the trapping potential. If we can always impart either an initial displacement or initial momentum to the atoms in the radial direction, the initial velocity problem is overcome because, by symmetry, there is no preferred directions for the principal axes. Assuming that the atoms start at the center of the trap, a reasonable assumption for our experiment, the initial velocity vector problem is solved because the Bragg splitting method always induces the initial motion in the radial direction.

Linear algebra techniques can be used to find the principal axes and the fundamental frequencies. The equation of motion of system in a potential described by Equation (4.2) is

$$\begin{pmatrix} \ddot{x} \\ \\ \ddot{y} \end{pmatrix} = -\frac{2k_B T}{m} \begin{pmatrix} a_{xx} & a_{xy}/2 \\ \\ a_{xy}/2 & a_{yy} \end{pmatrix} \begin{pmatrix} x \\ \\ y \end{pmatrix} \tag{4.3}$$

Seeking oscillating solutions of the form

$$q_j(t) = a_j e^{i(\omega t - \delta)} \tag{4.4}$$

where a_j are real amplitudes, δ is the phase offset, and q_j is a generalized coordinate representing x or y, we can find the oscillation frequency ω of the system by solving for the eigenvalues of the coefficient matrix in Equation (4.3). The principal axes are the eigenvectors of the same matrix. Solving for the eigenvalues and eigenvectors, we find

the oscillating frequencies and the principal axes to be

$$\omega_{\pm}^2 = \frac{k_B T}{m}\left(a_{xx} + a_{yy} \pm \sqrt{(a_{xx} - a_{yy})^2 + a_{xy}^2}\right) \tag{4.5}$$

$$\lambda_{\pm} = \left\{\frac{(a_{xx} - a_{yy})}{a_{xy}} \pm \frac{\sqrt{(a_{xx} - a_{yy})^2 + a_{xy}^2}}{a_{xy}}, 1\right\} \tag{4.6}$$

where $\omega_{\pm}$ denotes the eigenvalues, and $\lambda_{\pm}$ denotes the eigenvectors. For the ideal case, $a_{xx} = a_{yy} \equiv a$ and $a_{xy} = 0$, the eigenvalues become degenerate with the oscillating frequency $\omega = \frac{2k_B T}{m} a$ in all directions. The principal axes are undefined for the ideal case because any two orthogonal axes are principal axes. Asymmetry occurs when either $a_{xx} \neq a_{yy}$ or $a_{xy} \neq 0$.

In an asymmetric trap, we can expect observable behaviors that deviate from the behaviors found in an ideal symmetric trap. In addition to the trajectory's shape constantly changing for oscillation not aligned along a principal axis (as shown in Figure 1.3c), one can also observe beat patterns. As we can see from the fundamental oscillation frequencies described by Equation 4.5, in an asymmetric trap, the two fundamental oscillation frequencies are not degenerate. An oscillation along either principal axis results in the motion maintaining its shape, similar to how a pure state remains in the same state throughout its motion. An oscillation not parallel to a principal axis is expressed in terms of a superposition of two oscillations at the two fundamental frequencies. The superposition of the two frequencies results in an observable beat frequency. The beat pattern can be observed in our apparatus, see Figure 4.1, indicating that our science trap has asymmetric at the harmonic level.

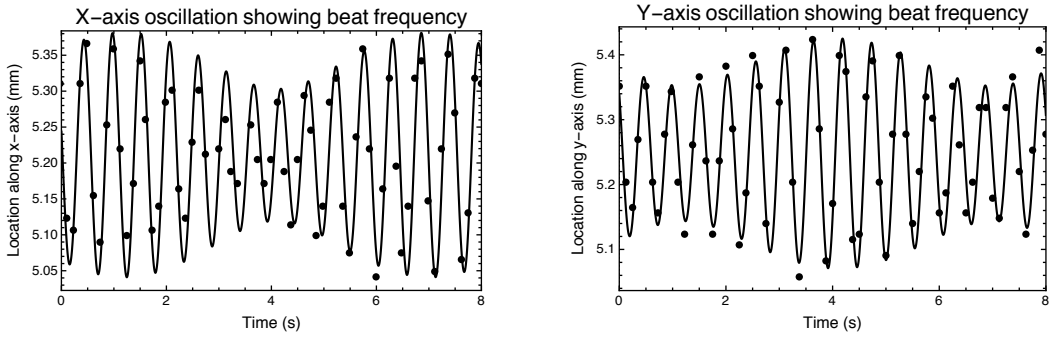

(a) Beat pattern along x axis **(b)** Beat pattern along y axis

Figure 4.1: Two diagrams showing beat pattern found when the trajectory of the trap was measured. The presence of the beat pattern suggests non-vanishing crossterms in the potential. The periods of oscillation in the x and y direction are 642.7 ms and 588.7 ms respectively. Fitting the beat pattern also allows us to determine the principal axes. When look down along the z-axis, one principal axis is found at 47 degrees counter-clockwise from the +x-axis. The other principal axis is orthogonal to the first one.

4.2 Achieving harmonic symmetry

For an atomic Foucault pendulum to work, We need the potential matrix in Equation (4.2) to be diagonal. The solution is to find some trap parameters which can be adjusted to make $a_1 = a_2$ and $a_3 = 0$. Instead of running the science trap with the nominal fields described in Section 2.1.3, we can easily make two modifications. First, we can use different amounts of bias current in different pairs of coils. Second, we can change the phase difference between the x and y bias fields. With these two modifications, the magnetic fields generated by the coil are

$$\vec{B}_{quad} = B_1' \cos\Omega_1 t \begin{pmatrix} x/2 \\ y/2 \\ -z \end{pmatrix} \tag{4.7}$$

$$\vec{B}_{bias} = B_0 \begin{pmatrix} (1 - \frac{\Delta}{2}) \sin \Omega_1 t \cos (\Omega_2 t + \delta) \\ (1 + \frac{\Delta}{2}) \sin \Omega_1 t \sin \Omega_2 t \\ \cos \Omega_1 t \end{pmatrix} \tag{4.8}$$

where B_0 is now the average bias field for the x and y coils, Δ gives the two horizontal coils different bias current, and δ imparts a phase offset to the x-coil.

With these modifications and the assumption that the modifications are small in magnitude, the time-averaged magnitude of the combined quad and bias field, which is proportional to the potential experienced by the atoms through Equation (2.3), is

$$\langle |\vec{B}| \rangle = B_0 \left[1 + \left(\frac{B_1'}{B_0} \right)^2 \left(\frac{7 + \Delta}{128} x^2 + \frac{7 - \Delta}{128} y^2 - \frac{\delta}{64} xy \right) \right] \tag{4.9}$$

Notice that we can adjust the diagonal terms using Δ. The off-diagonal term can be adjusted using δ.

To verify this effort, the atom cloud inside the magnetic atom trap is measured using tomographic fluorescence imaging as described in Chapter 3 as the relative bias current and phase between the x and y coils (Δ and δ respectively) are changed.

First, we adjust the current difference between the x and y coil pairs. The bias current through the y-coils is held constant, while that through the x-coils is varied. Fifty tomographic fluorescence images of the cloud at the height at $z = 0$ are obtained for each bias current setting. The images were analyzed according to the method described in Section 3.3. We find that the diagonal terms a_{xx} and a_{yy} are identical when the x-coils' current is 95% of that in the y-coils. We conclude that we can make the di-

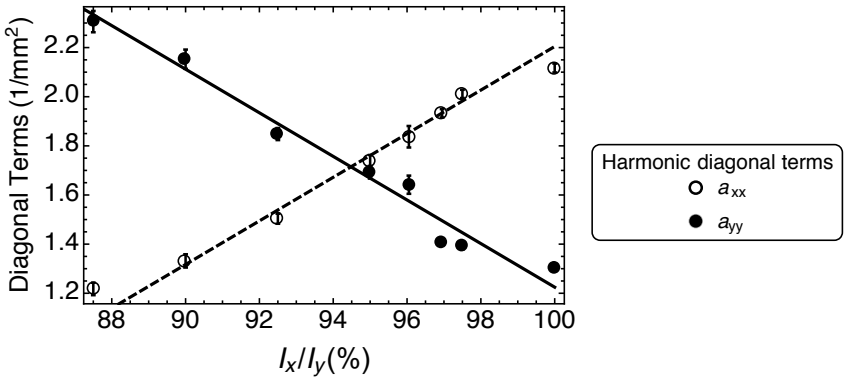

(a) The bias current along the x-direction is varied, while that along the y-direction is kept constant. When the current in the two directions differ greatly, such as on either end of the plot, clear asymmetry is observed. The two diagonal terms of the potential converges when the x-bias current is around 94.5% that of the y-current. Maximum current corresponds to 1.38 A in amplitude. The lines show the change in the harmonic terms as predicted by Equation (4.9).

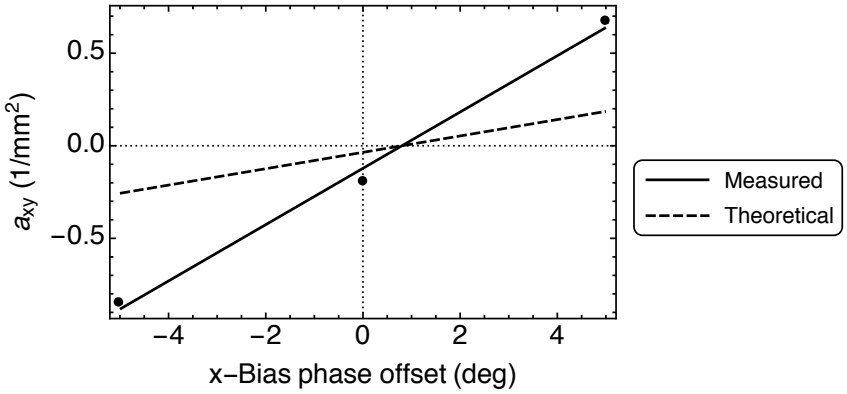

(b) The phase offset of the X-bias is varied while we measure about the a_{xy} coefficient in the trapping potential. The coefficient vanishes at 0.8 degrees phase offset. The linear model fit is justified through Equation (4.9). The linear fit to the measured data is $0.15(1)\delta - 0.12(5)$. The linear equation for the theoretical prediction is derived from Equation (4.9) and adjusting the offset to accommodate symmetry point happening away from zero degree phase offset. The theoretically predicted slope is 0.044, about a third of the measured value.

Figure 4.2: Two figures showing empirical evidence supporting Equation (4.9). In Figure 4.2a, the a_{xx} and a_{yy} coefficients of the potential can be made identical by changing the relative bias current between the two horizontal coil pairs. In Figure 4.2b, we can eradicate the a_{xy} term by a careful selection of the phase offset when the bias drive current signal is generated

agonal terms of the trapping potential equal by adjusting the difference between the bias current along the two horizontal directions.

Second, the phase offset of the y-bias current is adjusted. Since the x-coils and y-coils are being supplied by two function generators that are phase locked to one another, shifting the phase offset of the x-coils is done by simply adjusting the offset of the phase lock. A hundred tomographic images are obtained at each phase offset setting. Using linear model fit, we find that the cross term a_{xy} vanishes when the phase offset is 0.8 degrees. While qualitatively agreeing with our theoretical prediction, the rate of change in the cross terms $da_{xy}/d\phi$ is about three times larger than the rate predicted by Equation (4.9). We have no explanation for this difference beyond recognizing that our approximated model does not fully describe the science trap.

4.3 Acceptable level of harmonic asymmetry

In this section, we will calculate the maximum level of harmonic asymmetry allowed for implementation of an atomic Foucault pendulum. A trajectory initiated by a Bragg kick along the line making an angle θ_0 to the x-axis can be described as

$$\begin{aligned} x(t) &= a\cos\theta_0 \sin(\omega_+ t) \\ y(t) &= a\sin\theta_0 \sin(\omega_- t) \end{aligned} \tag{4.10}$$

where a is the maximum distance of from the origin, $\omega_\pm = \omega \pm \frac{\Delta\omega}{2}$ are the fundamental frequencies, ω is the average frequency. We assume that the motion has the principal axes along the x and y-axis and has no Foucault effect. We associate ω_+ with

the x-axis. In an asymmetric trap, the trajectory of the atoms is a precessing ellipse. If we always measure a trajectory, which starts at arbitrary time T, over a duration of one average oscillation period $2\pi/\omega$, we can simplify the equation above by defining $\Delta\omega T/2 \equiv \phi/2 \approx$ constant.

$$\begin{aligned} x(t) &= a\cos\theta_0 \sin\left(\omega t + \frac{\phi}{2}\right) \\ y(t) &= a\sin\theta_0 \sin\left(\omega t - \frac{\phi}{2}\right) \end{aligned} \tag{4.11}$$

Since the trajectory is an ellipse, we can describe it using a general ellipse equation

$$\frac{x^2}{(\cos\theta_0)^2} + \frac{y^2}{(\sin\theta_0)^2} - \frac{2xy\cos\phi}{\sin\theta_0\cos\theta_0} = a^2\sin\phi \tag{4.12}$$

which only describes one period oscillation starting at time T. The semi-major axis, the semi-minor axis, the eccentricity, and the rotation of the ellipse can be found from the above equation. Of particular interest is the angle that the semi-major axis makes with the $+x$-axis. In case of a small ϕ, this angle θ , expanded into a series up to the fourth order in ϕ, is

$$\Delta\theta = \theta - \theta_0 = -\frac{1}{8}\sin(4\theta_0)\phi^2 - \frac{1}{96}\sin 2\theta(\cos 2\theta - 3\cos 6\theta)\phi^4 \tag{4.13}$$

Note that the left hand side of the equation represents the rotation of the line of oscillation caused by asymmetry in the atom trap. This rotation can mask the rotation induced by the Foucault effect. For a single measurement of angle, the rotation is proportional to $(\Delta\omega)^2$.

We can decrease the sensitivity to $\Delta\omega$ by launching the atoms at two different angles that are 45° apart. If the rotation angles measured with the two launch angles are averaged, we get

$$\frac{1}{2}\left[\Delta\theta_{\theta_0} + \Delta\theta_{\theta_0+45^\circ}\right] = \frac{1}{64}\sin\left(8\theta_0\right)\phi^4 \tag{4.14}$$

With two launch angle averaging, the rotation of the line of oscillation is proprotional to the next order in ϕ^2. The rotation is now proportional to $(\Delta\omega)^4$.

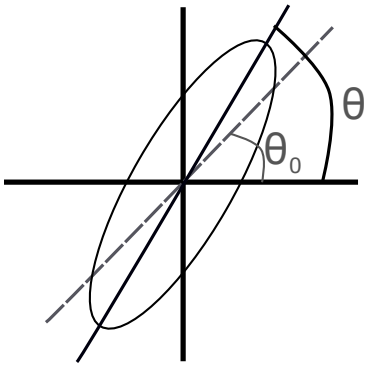

Figure 4.3: A diagram shows how angles are measured for trajectory analysis. The initial launch angle is θ_0, the angle of the elliptical trajectory at the time of measurement is θ.

To launch the atoms at 45° apart, we need two Bragg beams. Without loss of generality, we will label the two directions the 0° and 45° split. For a 0° split, a Bragg beam is retro-reflected back onto itself to create a standing off-resonant wave for Bragg scattering. For a 45° split, the reflected beam is blocked, and an extra beam illuminates the atoms in the direction perpendicular to the original Bragg beam. The two laser beams impose periodic potential on the atoms in the same direction as the sum of the two k-vectors of the two light beams, which is at 45° to the 0° split direction.

Requiring that the rotation caused by asymmetry be less than the amount of rotation caused by the Foucault effect at 60 seconds, our proposed duration for atomic Foucault pendulum, we can use Equation (4.13) and Equation (4.14) to calculate the maximally acceptable asymmetry. The calculated values do not depend on the principal angular frequencies, but only on the difference between them. For a single launch

angle measurement, the upper bound for harmonic asymmetry is $\Delta\omega = 0.0024$ s^{-1} at the worst possible launch angle of $\theta_0 = \pi/8$. For two launch angle averaging, the acceptable level of angular frequency difference is $\Delta\omega = 0.0107$ s^{-1} at the worst possible launch angle of $\theta_0 = \pi/16$. Given its better performance, the two launch angle averaging method is the only technique we will discuss going forward. We also solve the problem numerically to verify our result. The plot of acceptable difference in the two fundamental oscillating period can be seen in Figure 4.4.

For our typical trap frequency of 2 Hz, we can convert the acceptable values presented in Figure 4.4 to get the acceptable upper bound for the harmonic terms' coefficients as

$$\begin{aligned} |a_{xx} - a_{yy}| &\leq 0.0047 \text{ mm}^{-2} \\ |a_{xy}| &\leq 0.0094 \text{ mm}^{-2} \end{aligned} \tag{4.15}$$

which agree well with the limits calculated analytically. From the limits presented above, we can estimate the precisions we need to adjust the current and phase offset using the measurements presented in Figure 4.2. For the current offset, assuming the typical maximum current of 1.38 A in amplitude, we need to be able to control our current to within 700 μA of the symmetry point. We need to control our phase offset to within 0.06 degrees. Both of the precision requirements are challenging but certainly achievable with carefully designed circuits.

4.4 Conclusions

In this chapter, we have shown that our ideal model of the trapping potential, which predicts cylindrical symmetry, does not describe the magnetic atom trap. The asymmetry in the trap causes multiple observable phenomena: beat patterns and the existence of definite principal axes of motion. We can obtain the cylindrical symmetry in the harmonic terms by changing the relative bias currents and phase offset between the two horizontal coil pairs. We also established the minimum amount of symmetry needed for successful implementation of atomic Foucault pendulum.

In the next chapter, we will investigate higher order terms, the anharmonic terms, that hinder us from achieving an atomic Foucault pendulum. We will show that tomographic imaging technique can fully describe the higher order terms. We will verify the values obtained tomographically with oscillation measurement and numerical simulation of the trapping potential.

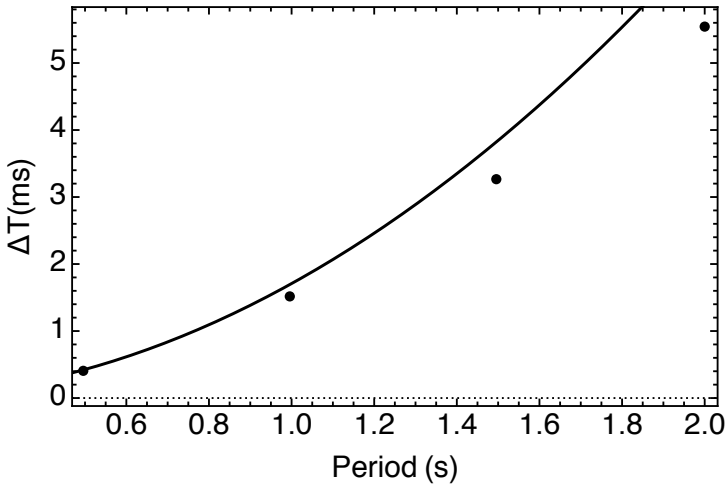

(a) Different in oscillation period between the two principal axes such that the change in angle is less than the rotation caused by the Foucault effect.

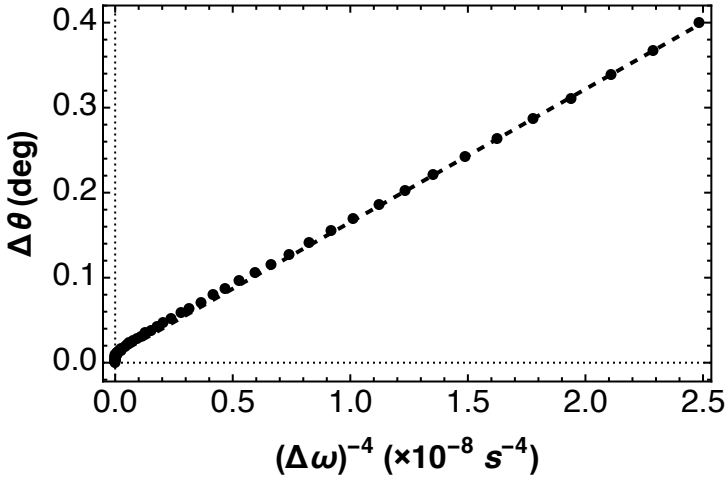

(b) $\Delta\theta$ average of two launch angles as a function of $\Delta\omega$

Figure 4.4: Two diagrams showing good agreement between the numerical result and and the analysis presented in this section. The coriolis force causing the Foucault effect is ignored. Figure 4.4a shows the maximally acceptable period difference for successful implementation of atomic Foucault pendulum. "Acceptable" is defined as the angle change at the time of measurement being less than the rotation that the Foucault effect would have caused. The line shows the calculated result using Equation (4.14). Figure 4.4b shows the line of oscillation rotation at 60 s oscillation time at various angular frequency. The rotation is proportional to the fourth-power of $\Delta\omega$ as suggested by Equation (4.14)

5

Anharmonic Terms

In the last chapter, we have discussed how we can approach cylindrical symmetry in the atom trap, up to the harmonic terms. In this chapter, we will discuss the effects of the higher-order, anharmonic terms on the motion. The cause of anharmonicity will be discussed. A simple example in 1D will be given to help explain the concept. The negative effects of anharmonicity on an atomic Foucault pendulum experiment will be shown. We will estimate the upper bound for the anharmonicity for a successful atomic Foucault pendulum implementation. Ultimately, the presence of a measurable anharmonicity currently prevents us from a successful imple-

mentation of an atomic Foucault pendulum. The tomographic method introduced in Chapter 3 allows us to measure all the terms in the trapping potential. We will investigate the anharmonicity of the magnetic atom trap using tomographic imaging. The measurement result will be presented. The result will be compared with other methods used to establish the values of the anharmonicity terms. The comparison will verify that the tomographic imaging technique is accurate, quick to implement, and reliable.

5.1 Anharmonicity

A potential affecting a motion can always be expanded into its Taylor's expansion. For small oscillation amplitude, it is generally adequate to keep only the first non-vanishing terms. These are usually the second-order terms (harmonic). The equation of motion for a harmonic potential is easily solved, well known and widely used [22, 21, 51]. More generally, the harmonic expansion cannot fully describe the motion, and higher order terms are needed. The higher order terms beyond the second-order are called the anharmonic terms.

To understand the effect of anharmonicity better, consider motion in one dimension. To reflect the polynomial described in Equation (3.7) and facilitate later comparison with our measurement results, we describe the potential as

$$U(x) = k_B T(ax^2 + bx^3 + cx^4) \tag{5.1}$$

where T is the temperature of the atom cloud and k_B is the Boltzmann's constant. The ax^2 term is harmonic, while the bx^3 and cx^4 terms are anharmonic. The Lagrangian

of this potential is

$$\mathcal{L} = \frac{1}{2}m\dot{x}^2 - k_B T(ax^2 + bx^3 + cx^4) \tag{5.2}$$

The equation of motion is

$$m\ddot{x} + 2k_B Tax = -3k_B Tbx^2 - 4k_B Tcx^3 \tag{5.3}$$

We present here the result demonstrated by Landau, but with our notation [21]. We seek a series solution of the form

$$\begin{aligned} x =& x^{(1)} + x^{(2)} + x^{(3)} \\ \omega =& \omega_0 + \omega^{(1)} + \omega^{(2)} \\ \omega_0 =& \sqrt{\frac{2k_B Ta}{m}} \\ x^{(1)} =& A\cos\omega t \end{aligned} \tag{5.4}$$

where A is the oscillation amplitude. With a properly selected origin for time, we can ignore the phase offset for $x^{(1)}$ without any loss of generality. For a series solution up to the third term in the series, we have

$$\omega = \sqrt{\frac{2k_B Ta}{m}} + A^2\sqrt{\frac{k_B T}{2am}}\left(\frac{3}{2}c - \frac{15}{8}\frac{b^2}{a}\right) + \mathcal{O}\left(A^3\right) \tag{5.5}$$

For small enough oscillation, the angular frequency ω remains constant. As the amplitude A is increased, the oscillation frequency is altered. Measuring the oscillation frequency change as a function of oscillation amplitude allows one to estimate the an-

harmonicity. This relationship could be used to characterize an atom trap.

While this calculation is straight forward in 1D, the situation in 2D or 3D is more complicated due to many factors including possible coupling between motion along different axes. Similarly obtaining the potential from an observed trajectory is generally difficult. For this reason, we use tomographic imaging technique as described in Section 3.2 for our study.

We hypothesize multiple factors that can lead to anharmonicity in the magnetic atom trap. First, even in the ideal case, the fields of Equation 2.7 and 2.8 do produce an anharmonic potential. We confirm this through numerical simulation. The result will be discussed later in Section 5.2. Second, the leads supplying the coils do contribute extra magnetic fields that can make the trapping potential asymmetric. Finally, environmental fields and gradients could countribute to the anharmonic terms as well.

5.2 Result and analysis

To measure the anharmonic terms, we follow the procedure outlined in Chapter 3. Knowing the temperature (measured in Section 3.4) and the atom cloud's profile measured from tomographic slices, we can relate the potential profile of the trap to the atom cloud through Equation (3.2). For example, the potential at a fixed height can be expressed by Equations (3.6) and (3.7). we obtain 100 tomographic slices at a fixed height $z = 0$ and calculate the coefficients a's, b's, and c's. The results are shown in the table below.

Coefficients	Values	Units
a_{xx}	1.73(6)	mm^{-2}
a_{yy}	1.52(4)	mm^{-2}
a_{xy}	-0.04(3)	mm^{-2}
b_{xxx}	0.072(5)	mm^{-3}
b_{yyy}	0.025(3)	mm^{-3}
b_{xyy}	-0.046(2)	mm^{-3}
b_{xxy}	-0.091(6)	mm^{-3}
c_{xxxx}	0.096(9)	mm^{-4}
c_{yyyy}	0.06(2)	mm^{-4}
c_{xxyy}	0.008(7)	mm^{-4}
c_{xyyy}	-0.31(8)	mm^{-4}
c_{xxxy}	-0.03(8)	mm^{-4}

Table 5.1: Table showing the coefficients in the potential measured through fluorescence tomographic imaging. The principal axes are aligned as shown in Figure 2.3

.

We check the validity of our measurement by comparing it to our results for how the oscillation frequency depends on the amplitude in a 1D case, first shown in Section 3.4. We also compare to a numerical simulation of the trapping potential.

We first verify our measurement of anharmonic terms by comparing the change in measured oscillation frequency to the change predicted based on Equation (5.5) and the coefficients obtained through measurements as shown in Table 5.1. The principal axis of the motion is along the $y = x$ line, with the axes defined as in Figure 2.3. The oscillation is induced by the kick coil. Since the oscillation is along the principal axis, the motion is approximately 1D. Consequently, the anharmonic terms affect the oscillation frequency in a predictable way, as shown in Equation (5.5). The potential coefficients shown in Table 5.1 are rotated to have one of the principal axes aligned with the $y = x$ line. The change in oscillation frequency can then be calculated. Figure 5.1 shows the comparison between the measured oscillation frequency and the predicted values. Given the reasonable agreement between the measurement and the calculated

values, we are confident in the accuracy of our tomographic techniques.

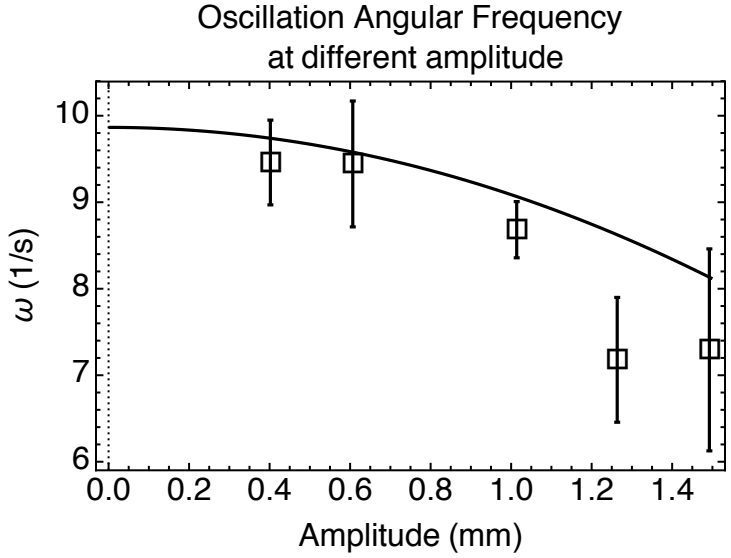

Figure 5.1: The plot shows the comparison between the directly measured and the tomographically determined values of the oscillation frequency at various oscillation amplitudes. The data points shown the values obtained empirically. The line shows the values derived from the potential terms shown in Table 5.1. The model agrees well with the measurement result, with χ^2 of 0.415.

The measured anharmonic terms are also comparable to the the similar terms obtained by numerical analysis of the magnetic atom trap's potential. A numerical analysis of the trap was performed by modeling each coil as fourteen concentric loops of varying sizes. While the actual coil has two spirals on each side of the base, the model still provides a good approximation [6]. The magnetic field created by each loop is calculated using elliptic integrals, derived from Biot-Savart law [52]. We have seen already [6] that the model is not very accurate in regards to the harmonic terms. To make a fair comparison, we adjust the model bias field to provide harmonic terms that match the experimental results (with an oscillation frequency of 1.6 Hz). The comparisons are presented in Table 5.2. The numerical model indicates negligible contribution from the third order terms and the non-symmetric anharmonic terms. The model results do not agree well, but do give the same order of magnitude, and show C_{xxyy} considerably

smaller than C_{xxxx} and C_{yyyy}.

Potential Terms	Tomography	Numerical result
c_{xxxx}	9.6(9)	4.1
c_{yyyy}	6(2)	4.1
c_{xxyy}	0.8(7)	-7.7

Table 5.2: Table showing the comparison of the anharmonic terms obtained by tomography and numerical simulation. The small amplitude oscillation frequency, instead of the running current in the science trap, between the measured result and the model are matched. All values are in ($\times 10^{-2}$ mm^{-4}) unit.

Rather than creating a tomographic slice at a fixed z, we can also obtain tomographic slices at varying heights. Various quantities can then be plotted as a function of z. The results are shown in Figure 5.2. Note the linear relationship between the harmonic a_{xx} and a_{yy} term as a function of height. The linear model suggests a coupling of x^2 and y^2 with z, which is expected since gravity breaks the potential symmetry along the z-axis. This evidence would be hard to obtain through oscillation trajectory analysis alone.

5.3 Acceptable level of anharmonicity

We can estimate the upper bound of the acceptable level of anharmonicity. There are methods for analytical estimation. For example, Synge and Griffith's treatment of a sperical pendulum [53] and a series approximation as demonstrated by Landau [21] can be combined to present a series solution of the trajectory in 3D. We use a numerical method. By numerically solving the equations of motion from a potential similar to that in Equations (4.1) and (4.2) with the addition of anharmonic terms, we can find the maximum value allowed for the anharmonic coefficients for successful implementation of an atomic Foucault pendulum. Similar to the harmonic terms limitation, an

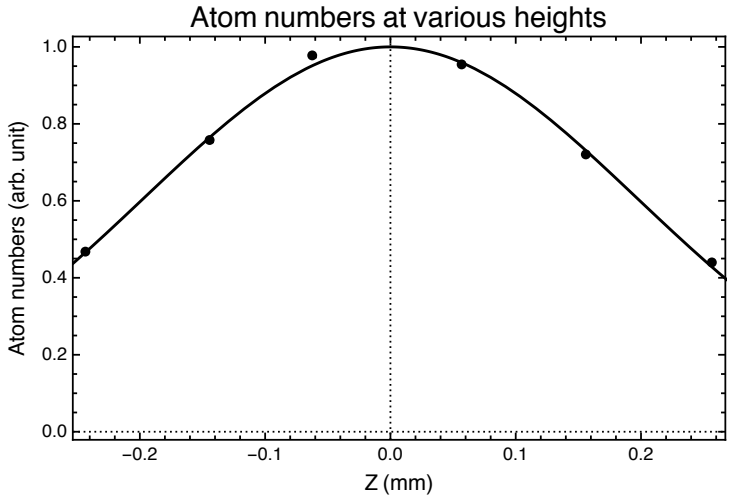

(a) Atom number at various heights with Gaussian fit

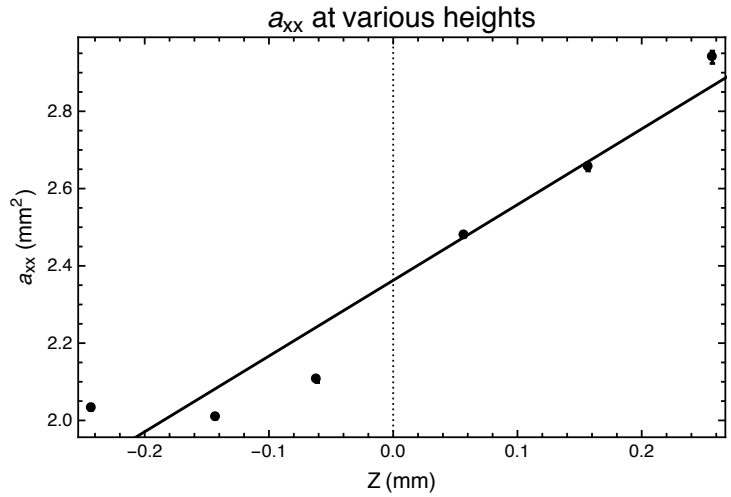

(b) a_{xx} at various heights with linear fit

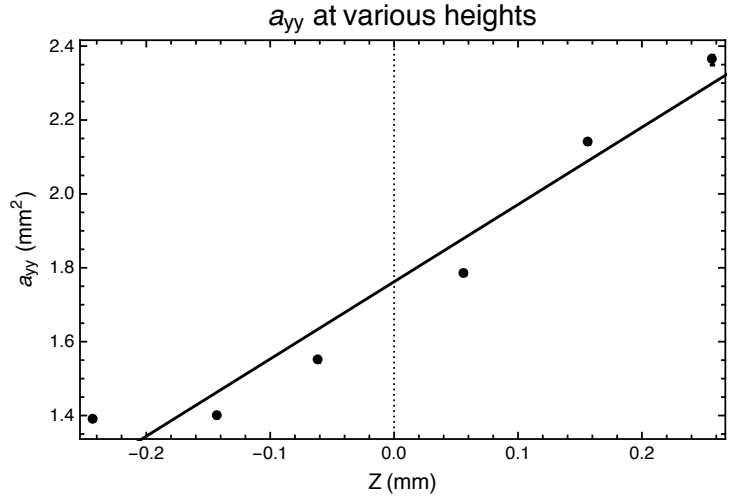

(c) a_{yy} at various heights with linear fit

Figure 5.2: Figures showing various quantities at various heights as measured tomographically.

average of two launch angles separated by 45 degrees yields a better result than a single launch angle. Using the potential of which the harmonic terms have complete symmetry and the interested term is the only non-vanishing term, the limits on the anharmonic terms are found to be

$$\begin{aligned} |b| &< 0.055 \ \text{mm}^{-3} \\ |c| &< 0.0013 \ \text{mm}^{-4} \end{aligned} \tag{5.6}$$

where b represents the terms proportional to the cubic terms in spatial dependence and c represents the terms proportional to the fourth-order terms. In general, we have found little variation between the different terms in the same order. The values above represents the most stringent condition needed. The measured coefficients shown in Table 5.1 exceed the presented limits. It is therefore clear that a method to adjust the anharmonic terms will be required if the Foucault experiment is to succeed.

5.4 Conclusions

In this chapter, we have shown that anharmonic terms are present in our trapping potential. We have presented an effective and accurate way to measure the terms through tomographic imaging techniques. The measurement results were verified by another measurement and a numerical simulation of the science trap. The acceptable limits on the anharmonic terms were established through numerical simulation. With the presence of the anharmonic terms, we conclude that, unless further modifications are made, implementing an atomic Foucault pendulum in the magnetic atom trap is unlikely.

6

Conclusion

While we were not able to implement an atomic Foucault pendulum, our effort in developing a tomographic imaging system will help us quantitatively characterize the science trap in the future. Having developed the technique, we have found some invaluable information that would not have been possible to obtain without great difficulty.

One, we have confirmed that the trap can be made harmonically cylindrically symmetric through adjusting the relative bias current and phase between the x and y-coils. The tomographic technique can also help determine the orientation of the prin-

cipal axes in the science trap.

Two, the tomographic technique allows us to quantitatively measure the anharmonicity of the trapping potential. Additionally, the anharmonic terms can be measured as a function of vertical height, which provides extra information unobtainable through other methods we have developed in the past. The coupling between the horizontal and vertical directions is crucial for successful implementation of the improved Gravimeter proposed by Horne [6].

Three, knowing the anharmonicity allows us to better predict the period of oscillation of atom clouds in the science trap as a function of oscillating amplitude. Knowing the period more precisely is crucial for high-precision measurements intended to be implemented in the trap, such as the improved Sagnac interferometer proposed by Horne [6].

A few methods have been proposed for reducing the amount of asymmetry in the science trap. External induction coils can be installed to produce the proper bias field to cancel out the asymmetry. A major drawback of installing external coils is the physical space required by the coils. The extra coils also limit optical access to the atoms. The most likely method that we are actively pursuing is using arbitrary waveform to drive the science trap coils. Rather than using simple sinusoidal signals, a specially designed waveform with higher harmonic terms can be used for each of the coil pair. With phase locking to the current bias current, the arbitrary waveform can provide varying current along different axes of the trap to reduce the magnitude of the asymmetric terms.

References

[1] C. Cohen-Tannoudji and D. Guéry-Odelin, *Advances in Atomic Physics*. World Scientific Publishing Co. Pte. Ltd., 2011.

[2] V. S. Bagnato, K. M. F. Magalhães, J. A. Seman, E. A. L. Henn, and E. R. F. Ramos, "Introduction to the basic-concepts of Bose-Einstein condensation," in *AIP Conference Proceedings*, vol. 994, pp. 79–97, 2008.

[3] C. J. Pethick and H. Smith, *Bose–Einstein Condensation in Dilute Gases*. Cambridge: Cambridge University Press, jun 2008.

[4] A. Sørensen, L.-M. Duan, J. I. Cirac, and P. Zoller, "Many-particle entanglement with Bose–Einstein condensates," *Nature*, vol. 409, pp. 63–66, jan 2001.

[5] K. J. Hughes, J. H. T. Burke, and C. a. Sackett, "Suspension of Atoms Using Optical Pulses, and Application to Gravimetry," *Physical Review Letters*, vol. 102, p. 150403, apr 2009.

[6] R. Horne, *A Cylindrically Symmetric , Magnetic Trap for Bose-Einstein Condensate Atom A Cylindrically Symmetric, Magnetic Trap for Bose-Einstein Condensate Atom Interferometry Applications*. PhD thesis, University of Virginia, 2015.

[7] R. Leonard, *High precision measurement of the D-line tune-out wavelength in 87Rb using a Bose-Einstein condensate interferometer*. PhD thesis, University of Virginia, 2016.

[8] R. H. Leonard and C. A. Sackett, "Effect of trap anharmonicity on a free-oscillation atom interferometer," *Physical Review A*, vol. 86, p. 043613, Oct 2012.

[9] J. P. Brantut, J. F. Clément, M. R. De Saint Vincent, G. Varoquaux, R. A. Nyman, A. Aspect, T. Bourdel, and P. Bouyer, "Light-shift tomography in an optical-dipole trap for neutral atoms," *Physical Review A - Atomic, Molecular, and Optical Physics*, vol. 78, no. 3, pp. 78–81, 2008.

[10] Wikipedia, "List of Foucault Pendulums," 2016.

[11] L. Baker, J. A. Gregory, and Blackburn, "The Pendulum : A Case Study in Physics," in *The Pendulum : A Case Study in Physics*, ch. 4, Oxford, Great Britain: Oxford University Press, 2005 ed.

[12] J. B. Hart, "A simple geometric model for visualizing the motion of a Foucault pendulum," *American Journal of Physics*, vol. 55, no. 1, p. 67, 1987.

[13] J. von Bergmann and H. von Bergmann, "Foucault pendulum through basic geometry," *American Journal of Physics*, vol. 75, no. 10, p. 888, 2007.

[14] D. Condurache and V. Martinusi, "Foucault Pendulum-like problems: A tensorial approach," *International Journal of Non-Linear Mechanics*, vol. 43, pp. 743–760, oct 2008.

[15] G. I. Opat, "The precession of a Foucault pendulum viewed as a beat phenomenon of a conical pendulum subject to a Coriolis force," *American Journal of Physics*, vol. 59, no. 9, p. 822, 1991.

[16] D. Olenici and A. F. Pugach, "Precise Underground Observations of the Partial Solar Eclipse of 1 June 2011 Using a Foucault Pendulum and a Very Light Torsion Balance," *International Journal of Astronomy and Astrophysics*, vol. 02, no. 04, pp. 204–209, 2012.

[17] R. Snieder, C. Sens-Schönfelder, E. Ruigrok, and K. Shiomi, "Seismic shear waves as Foucault pendulum," *Geophysical Research Letters*, vol. 43, pp. 2576–2581, Mar 2016.

[18] D. Senkal, A. Efimovskaya, and A. Shkel, "Dual Foucault Pendulum gyroscope," in *2015 Transducers - 2015 18th International Conference on Solid-State Sensors, Actuators and Microsystems (TRANSDUCERS)*, pp. 1219–1222, IEEE, jun 2015.

[19] I. P. Prikhodko, S. A. Zotov, A. A. Trusov, and A. M. Shkel, "Foucault pendulum on a chip: Rate integrating silicon MEMS gyroscope," *Sensors and Actuators A: Physical*, vol. 177, pp. 67–78, apr 2012.

[20] C. L. Strong, "How to make a pendulum that will demonstrate the rotation of the earth," *The Amateur Scientist*, pp. 115–124, 1958.

[21] L. D. Landau and E. M. Lifshitz, *Mechanics*. New York: Pergamon Press, 2nd ed., 1982.

[22] S. T. Thornton and J. B. Marion, *Classical dynamics of particles and systems*, vol. 281. Cengage Learning, 5th ed., 2003.

[23] H. Goldstein, C. P. Poole Jr., and J. L. Safko, *Classical mechanics*. Pearson Education, 3rd ed., 2011.

[24] B. Pippard, "Foucault's pendulum," *Royal Institution Proceedings*, vol. 63, pp. 87–100, 1991.

[25] T. Arpornthip, C. A. Sackett, and K. J. Hughes, "Vacuum-pressure measurement using a magneto-optical trap," *Physical Review A*, vol. 85, p. 033420, Mar 2012.

[26] E. A. Salim, J. DeNatale, D. M. Farkas, K. M. Hudek, S. E. McBride, J. Michalchuk, R. Mihailovich, and D. Z. Anderson, "Compact, microchip-based systems for practical applications of ultracold atoms," *Quantum Information Processing*, vol. 10, pp. 975–994, dec 2011.

[27] M. R. Matthews, B. P. Anderson, P. C. Haljan, D. S. Hall, C. E. Wieman, and E. A. Cornell, "Vortices in a Bose-Einstein Condensate," *Physical Review Letters*, vol. 83, pp. 2498–2501, Sep 1999.

[28] H. J. Lewandowski, D. M. Harber, D. L. Whitaker, and E. a. Cornell, "Simplified system for creating a Bose-Einstein condensate," *Journal of Low Temperature Physics*, vol. 132, no. 5-6, pp. 309–368, 2003.

[29] H. J. Metcalf and P. van der Straten, *Laser cooling and trapping*. New York: Springer, 1999.

[30] C. J. Dedman, J. Nes, T. M. Hanna, R. G. Dall, K. G. H. Baldwin, and A. G. Truscott, "Optimum design and construction of a Zeeman slower for use with a magneto-optic trap," *Review of Scientific Instruments*, vol. 75, no. 12, pp. 5136–5142, 2004.

[31] E. L. Raab, M. Prentiss, A. Cable, S. Chu, and D. E. Pritchard, "Trapping of Neutral Sodium Atoms with Radiation Pressure," *Physical Review Letters*, vol. 59, no. 23, pp. 2631–2634, 1987.

[32] C. G. Townsend, N. H. Edwards, C. J. Cooper, K. P. Zetie, C. J. Foot, A. M. Steane, P. Szriftgiser, H. Perrin, and J. Dalibard, "Phase-space density in the magneto-optical trap," *Physical Review A*, vol. 52, no. 2, pp. 1423–1440, 1995.

[33] J. M. Reeves, *An Atom Waveguide For Interferometry With A Bose-Einstein Condensate of 87Rb.* PhD thesis, University of Virginia, 2006.

[34] D. W. Sesko, T. G. Walker, and C. E. Wieman, "Behavior of neutral atoms in a spontaneous force trap," *Journal of the Optical Society of America B*, vol. 8, no. 5, p. 946, 1991.

[35] T. Walker, D. Sesko, and C. Wieman, "Collective behavior of optically trapped neutral atoms," *Physical Review Letters*, vol. 64, no. 4, pp. 408–411, 1990.

[36] D. A. Steck, "Quantum and Atom Optics," 2007.

[37] W. H. Wing, "On neutral particle trapping in quasistatic electromagnetic fields," *Progress in Quantum Electronics*, vol. 8, pp. 181–199, jan 1984.

[38] C. Adams and E. Riis, "Laser cooling and trapping of neutral atoms," *Progress in Quantum Electronics*, vol. 21, no. 1, pp. 1–79, 1997.

[39] W. Ketterle, D. S. Durfee, and D. M. Stamper-Kurn, "Making, probing and understanding Bose-Einstein condensates," *Proceedings of the International School of Physics "Enrico Fermi"*, p. 67, 1999.

[40] J. Mitschele, "Beer-Lambert Law," *Journal of Chemical Education*, vol. 73, p. A260, nov 1996.

[41] C. J. Foot, *Atomic Physics*. New York: Oxford University Press, 2010.

[42] P. J. Martin, B. G. Oldaker, A. H. Miklich, and D. E. Pritchard, "Bragg scattering of atoms from a standing light wave," *Physical Review Letters*, vol. 60, no. 6, pp. 515–518, 1988.

[43] O. Garcia, B. Deissler, K. J. Hughes, J. M. Reeves, and C. A. Sackett, "Bose-Einstein-condensate interferometer with macroscopic arm separation," *Physical Review A*, vol. 74, p. 031601, sep 2006.

[44] K. J. Hughes, B. Deissler, J. H. T. Burke, and C. A. Sackett, "High-fidelity manipulation of a Bose-Einstein condensate using an optical standing wave," *Physical Review A*, vol. 76, p. 035601, sep 2007.

[45] M. Kozuma, L. Deng, E. W. Hagley, J. Wen, R. Lutwak, K. Helmerson, S. L. Rolston, and W. D. Phillips, "Coherent Splitting of Bose-Einstein Condensed Atoms with Optically Induced Bragg Diffraction," *Physical Review Letters*, vol. 82, pp. 871–875, feb 1999.

[46] E. Oh, *Asymmetric Splitting of Bose-Einstein Condensate*. PhD thesis, University of Virginia, 2014.

[47] J. T. Littleton and M. L. Durizsch Littleton, "Conventional Tomography," 1996.

[48] D. A. Steck, "Rubidium 87 D Line Data," *Journal of Geophysical Research*, vol. 2009, no. 2, p. 31, 2010.

[49] R. K. Pathria and P. D. Beale, *Statistical mechanics*. Butterworth-Heinemann publications, 3rd ed., 2011.

[50] R. H. Landau and M. J. Paez, *Computational Physics: Problem solving with computers*. New York: John Wiley & Sons, INc., first ed., 1997.

[51] J. Taylor, *Classical Mechanics*. United States: University Science Books, 2005.

[52] J. D. Jackson, *Classical Electrodynamics*. New York: John Wiley & Sons Ltd., 1962.

[53] J. L. Synge and B. A. Griffith, *Principles of Mechanics*. New York: McGraw-Hill Book Company, Inc., second edi ed., 1949.